UNIVERSITY OF CALIFORNIA SAN DIEGO

Ultrafast spectroscopy for new materials

A Thesis submitted in partial satisfaction of the requirements for the degree Master of Science

in

Chemistry

by

Liying Chen

Committee in charge:

Professor Wei Xiong, Chair
Professor Shaowei Li
Professor Alina Schimpf

2021

The thesis Liying Chen is approved, and it is acceptable in quality and form for publication on microfilm and electronically.

University of California San Diego

2021

TABLE OF CONTENTS

Thesis Approval Page iii

Table of Contents iv

List of Abbreviations vii

List of Figures ix

List of Scheme xiii

Acknowledgements xiv

Abstract of the Thesis xvi

Chapter 1 Ambient Temperature $Cr(CO)_3(\eta^6$-naphthalene)-Mediated 1,3-Dien-5-ynes Cycloaromatization 1

1-1 Introduction 2

1-2 Attempts in mediating dienyne cyclization 3

1-3 Mechanistic investigation and kinetic study with Fourier-transform infrared spectroscopy (FT-IR) 11

1-4 2D-IR in determining intermediates 19

1-5 Proposed Mechanism 22

1-6 Conclusion and Future work 23

1-7 Experimental 24

1-7-1 General procedures 24

1-7-2 FT-IR and 2D-IR 25

1-8 Acknowledgments 27

1-9 References 28

Chapter 2 Strain-Induced ferroelectricity in metal halide perovskites 30

2-1 Abstract 31

2-2 Introduction..... 32

2-3 Strained α-$FAPbI_3$ Single Crystalline Layer Structure..... 33

2-4 Ferroelectricity in α-$FAPbI_3$ 36

2-5 Strain-induced Ferroelectricity Origin 41

2-6 Conclusion 47

2-7 Methods..... 48

2-7-1 Transient IR Absorption 48

2-8 Acknowledgements 50

2-9 References 51

2-10 Supplemental information 55

2-10-1 Wobbling in a Cone/Jump motion 55

2-10-2 SI References ……..…….... 59

Chapter 3 Ultrafast interfacial charge transfer revealed by transient vibrational sum frequency generation spectroscopy…….. 61

3-1 Introduction ...…… 62

3-2 Current result …… 65

3-3 Future goal……. 68

3-4 Acknowledgments ……... 70

3-5 References ……... 71

LIST OF ABBREVIATIONS

2DIR	Two-dimensional infrared spectroscopy
α-$FAPbI_3$	α-Formamidinium lead iodide
CPMD	Car-Parrinello molecular dynamics
DFT	Density function theory
DFG	Difference frequency generation
DSC	Differential Scanning Calorimetry
ESA	Excited state absorption
FET	Field-effect transistor
GSB	Ground state bleach
ITC	inverse temperature growth
LO	Local oscillator
MCT	Mercury-Cadmium-Telluride
$MAPbCl_xBr_{3-x}$	Methylammonium lead chloride/bromide
$MAPbI_3$	Methylammonium lead iodide
NVM	Non-volatile memory
OPA	Optical parametric amplifier

SE	Stimulated emission
Tr EFI SFG	Time-resolved electric-field-induced sum-frequency generation
Tr EFI-HD SFG	Time-resolved electric-field-induced heterodyne sum frequency generation
TSDC	Thermally stimulated depolarization current
VSFG	Vibrational sum frequency generation spectroscopy
XPS	X-ray photoelectron spectroscopy

LIST OF FIGURES

Figure 1-1 X-ray crustal structure of 12 …….. 8

Figure 1-2 FTIR spectrum for isolated reactant and product ……..... 11

Figure 1-3 FT-IR monitored reaction of 4 with 1 in a 10:1 mole ratio in THF…... 12

Figure 1-4 FT-IR spectrum for control experiment in atmosphere ……. 13

Figure 1-5 FTIR monitored reaction of 18 with 1 in a 10:1 mole ratio in THF 14

Figure 1-6 FTIR monitored reaction of 4 with 1 in a 10:1 mole ratio in 2,5-dimethyl tetrahydrofuran ……. 15

Figure 1-7 Time trace for reactant, intermediate and product …..…….. 16

Figure 1-8 2DIR spectrum for reactant, first hour of reaction and product …… 19

Figure 1-9 2DIR spectrum cut at 1883cm^{-1} fitted with Gaussian function ..…….. 20

Figure 1-10 2DIR spectrum cut at 1960cm^{-1} fitted with Gaussian function ……. 20

Figure 1-11 Speculative mechanism of 1 mediated dienyne cyclization ……..... 22

Figure 1-12 Scheme of the 2D-IR set up in this study ..…… 26

Figure 2-1 Strained α-$FAPbI_3$ Structural Characterization ……..... 35

Figure 2-2 TSDC measurement ……... 40

Figure 2-3 Ferroelectricity and molecular origin ……..... 46

Figure 2-4 Scheme for transient IR absorption in this study ……... 49

Figure 2-SI-1 Calculated anisotropy decay lifetime under different time scale …….. 58

Figure 3-1 Band alignment for P3HT and BBL ……..... 64

Figure 3-2 Tr VSFG dynamic and power dependent result ……..... 66

Figure 3-3 Globle analysis ……..... 67

Figure 3-4 Schematic of the transient HD VSFG spectrometer setup …….. 68

LIST OF SCHEME

Scheme 1-1 Speculative mechanism of Ru compound…….. 2

Scheme 1-2 Thermal Hopf/Dienyne/enediyne cyclization……..... 2

Scheme 1-3 Bergman cyclization triggerd by $Cr(CO)_3$..…….. 3

Scheme 1-4 Two proposed mechanistic pathways in Cr ……... 5

Scheme 1-5 1 mediated electrocyclization of 4 and 6..... 6

Scheme 1-6 Synthesis of 8,9 and 1 mediated electrocyclization..…… 8

Scheme 1-7 1 mediated electrocyclization of 14……. 9

Scheme 1-8 1 mediated electrocyclization of 15……. 9

Scheme 1-9 18 and 19 failed to cyclize when reacting with 1…….. 10

Scheme 1-10 Proposed Mechanism…….. 11

ACKNOWLEDGMENTS

I would like to sincerely thank my thesis advisor Prof. Wei Xiong for his guidance throughout my Ph.D. study in his group. I would also like to thank my thesis committee members: Professor Shaowei Li and Professor Alina Schimpf for their help and suggestions.

Prof. Joseph O'Connor, and his graduate student Dr. Han Steger are acknowledged for material preparation in chapter 1. Prof. Sheng Xu, and his graduate student Dr. Yimu Chen are acknowledged for material preparation in chapter 2. Chenglai Wang is acknowledged for working together on project in chapter 3. Dr. Bo Xiang, Dr. Jiaxi Wang, Dr. Yingmin Li, Dr Haoyuan wang, Wenfan Chen, Jackson Wagner,Zimo Yang, Chenglai Wang, Garret Wiesehan for their support and as companions in Xiong's lab.

Finally, without my family members: Yuanlong Chen (Father), Xiaohong Wang (Mother), and girlfriend Zixuan Wang's companionship and support, none of this would have been possible.

The material in Chapter 1, is a reprint of the manuscript currently under preparation for publication with the following authors: Chen, Liying; Steger, Han; Baldridge, Kim K.; Xiong, Wei.; O'Connor, Joseph M. The thesis author was the primary investigator and author of this material.

The material in Chapter 2, is currently under preparation for publication with the following authors.: Chen*, Yimu; Zhang Ruiqi*, Chen, Liying, Saiful, Islam, Xiong Wei, Xu Sheng. The thesis author was the secondary investigator and author of this material.

The material in Chapter 3, is an ongoing project with following people: Chen, Liying, Wang, Chenglai under Dr Wei Xiong’s guidance.

ABSTRACT OF THE THESIS

Ultrafast Spectroscopy for New Materials

by

Liying Chen

Master of Science in Chemistry

University of California San Diego, 2021

Professor Wei Xiong, Chair

New materials are fundamental for modern industry. Novel materials are often composed with complex compositions and interfaces. Therefore, understanding the structure and dynamics of these new materials is important. In this thesis, we apply

advanced spectroscopy to study the structure and dynamic information of some novel materials.

In chapter 1, We report a chromium complex mediator, $Cr(CO)_3(\eta_6$-naphthalene), that mediates the traditional thermal dienyne cyclization at ambient temperature. We investigate mechanism and kinetic of this novel reaction by Fourier-transform infrared spectroscopy (FT-IR) and Static 2D IR spectroscopy. After studying the structure information of new chemical compound, we noticed that dynamic process can help us understand the system parameters changing over time. In chapter 2, we performed transient IR absorption to understand the cation rotation in a strain induced α-formamidinium lead iodide (α-$FAPbI_3$) system. Through transient IR absorption measurement, we demonstrate that the ferroelectricity generated in the strained α-$FAPbI_3$ owes to the inorganic framework atom displacement generated from the lead-iodide bonds with neglectable influence of freely-rotational FA^+ molecules under room temperature. After study the dynamic of novel material, we found out that molecule conformation at interface greatly influence the performance of materials. Therefore, in chapter 3, we develop a surface/interface sensitive technique called time-resolved electric-field-induced heterodyne sum frequency (Tr EFI-HD SFG) spectroscopy to follow the charge transfer process at interfaces. Currently, we study the interface which composed of acceptor polymer and donor polymer. We plan to extract the implicit molecular dynamics by transient HD VSFG.

Chapter 1 Ambient temperature $Cr(CO)_3(\eta^6$-naphthalene)-mediated 1,3-dien-5-ynes cycloaromatization.

1. Introduction.

Since the initial report in 1969,[1,2] dienyne/enediyne cyclization has generated significant interest and provided promising new applications to the current synthetic methodology.[3,4] However, high activation energy barrier of the thermal dienyne/enediyne cyclization requires high reaction temperature (~300 °C) (Scheme 1-

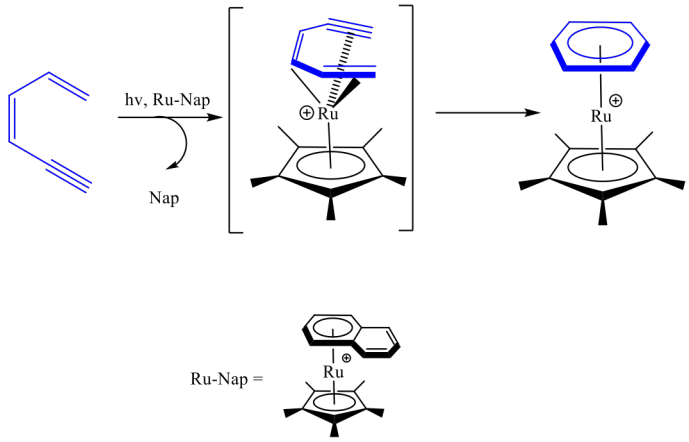

Scheme 1-1: Speculative mechanism of $Cp^*Ru^+(\eta^6$-dienyne) mediated dienyne cyclization.

1).[1,2,5] To address this drawback, Dr. Oconnor's laboratory has examined a variety of ruthenium complexes with three facial coordination sites and successfully triggered the

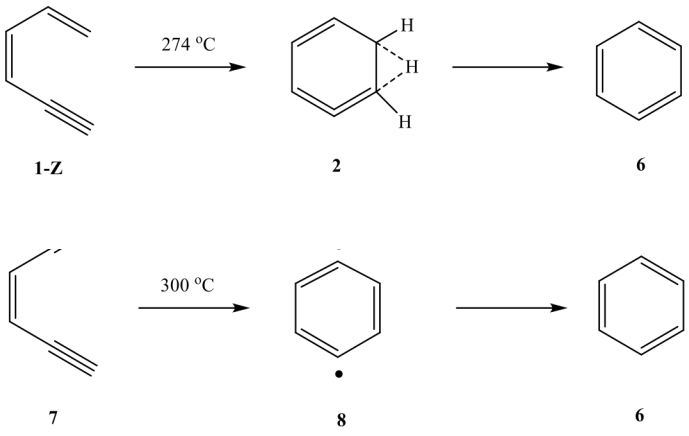

Scheme 1-2: Top: Thermal Hopf/dienyne cyclization under. Bot: Thermal Bergman/enediyne

cyclization at ambient temperature with excellent yields (Scheme 3-1).[6-8] However, considering the lack of stability with respect to oxygen and moisture as well as the high cost of ruthenium, we investigated the possibility of triggering the Hopf dienyne/enediyne cyclization by using more cost-efficient transition metal complexes(Scheme 1-2). The reactivity of hexahepto chromium complexes coordinated to the unsaturated carbon-carbon bonds has been extensively studied.[9-11]

Kundig and his group reported the first example of triggering Bergman cyclization with a $Cr(CO)_3(\eta^6$-napthelene) (**1**) complex at ambient temperature (Scheme1-3).

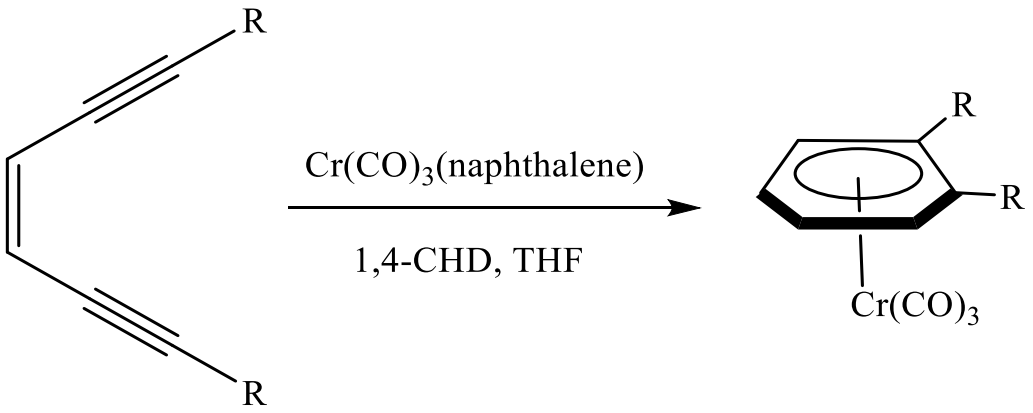

2

Scheme 1-3: Bergman cyclization triggered by $Cr(CO)_3$ under ambient temperature

Substrate **2** undergoes electrocyclization under room temperature in the coordination solvent THF. The yield significantly improved with the addition of a hydrogen source

1,4-CHD (Scheme 1-3). This reaction was not observed in a non-coordination solvent or with a bulky terminal substituent. Two mechanistic pathways (Scheme 1-4) were introduced in his work, while path A described a direct cyclization between C1 and C6 and B described oxidative coupling followed by reductive elimination and bond hemolysis. DFT computation methods suggested that Path B is unfavorable, with a comparison of 80.4 kcal/mol to 16.7 kcal/mol in activation energy barrier. Their work pointed out that the $Cr(CO)_3(\eta^6$-enediyne) complex is the crucial pathway that leads to cyclization. The formation of a benzene diradical intermediate was confirmed by a good match between experimental and simulated EPR spectra of the triplet p-benzyne biradical. Kundig's work demonstrated the viability of a chromium mediated variant to ruthenium presented by O'Connor's lab and its key intermediate benzyne biradical was observed to lie on the reaction pathway.

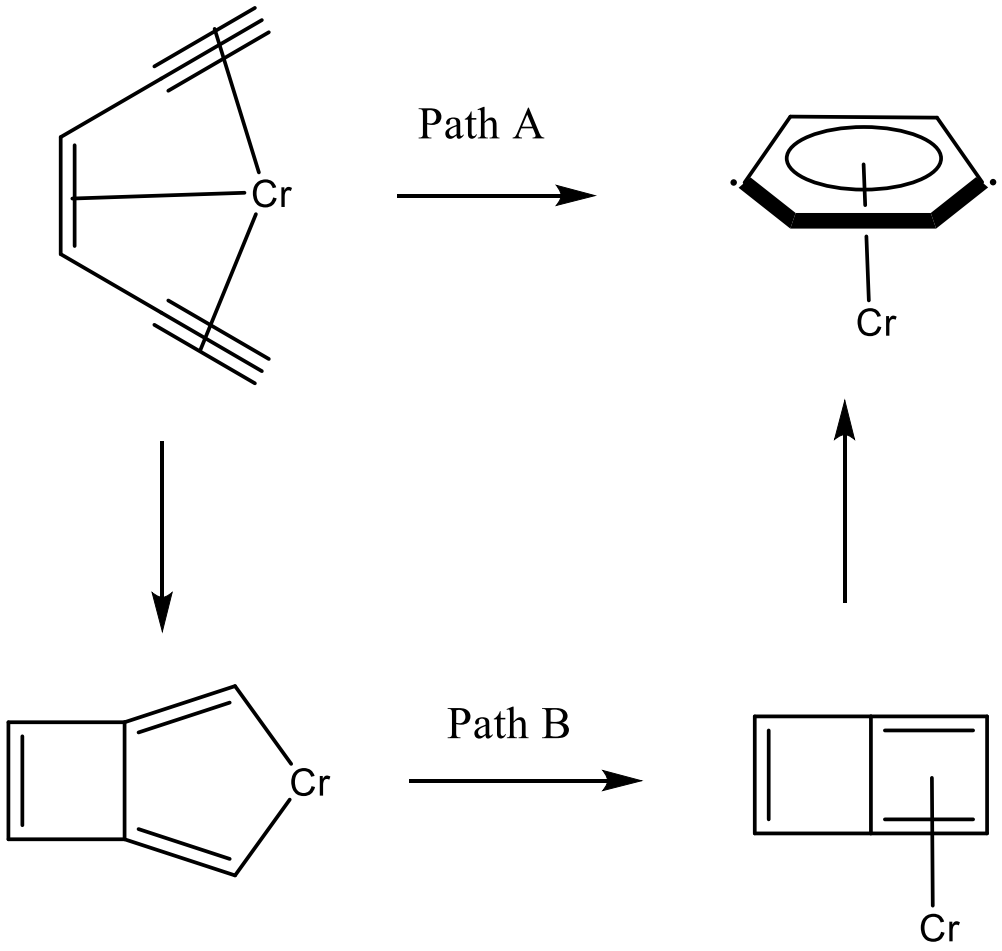

Scheme 1-4: Two proposed mechanistic pathways in Cr triggered Bergman cyclization

Encouraged by his work, we were excited to examine the capability with **1** in dienyne cyclization. Although the two cyclizations undergo different pathways, we believe that the hexahepto is the crucial intermediate in both electro cyclizations. Thus, we are expecting to see a Hopf cyclization that can be triggered with **1**.

2. Attempts in mediating dienyne cyclization.

Previously reported by our group, [Cp*Ru^{+}(η^6-naphthalene)][PF_6] (**3**) undergoes photon triggered naphthalene dissociation in coordinating solvent. A speculative intermediate [Cp*Ru^{+}(η^6-dienyne)]PF_6 was then formed followed by the cyclization of dienyne.[13] In comparison to **3**, arene dissociation of **1** occurs without the presence of a photon. Thus, a $Cr(CO)_3$(η^6-dienyne) intermediate can be reasoned and likely leads to the successful cyclization. Our study began with treating dienyne **4** with $Cr(CO)_3$(η^6-dienyne) in THF. After 16 hours, a product that exhibits an identical spectroscopic property to those previously reported was isolated via chromatography and was identified as **5,** which was obtained in a yield of 51 %. The reaction of **6** and $Cr(CO)_3$(η^6-naphthalene) led to the formation of the product **7**, which was isolated at a 43 % yield.

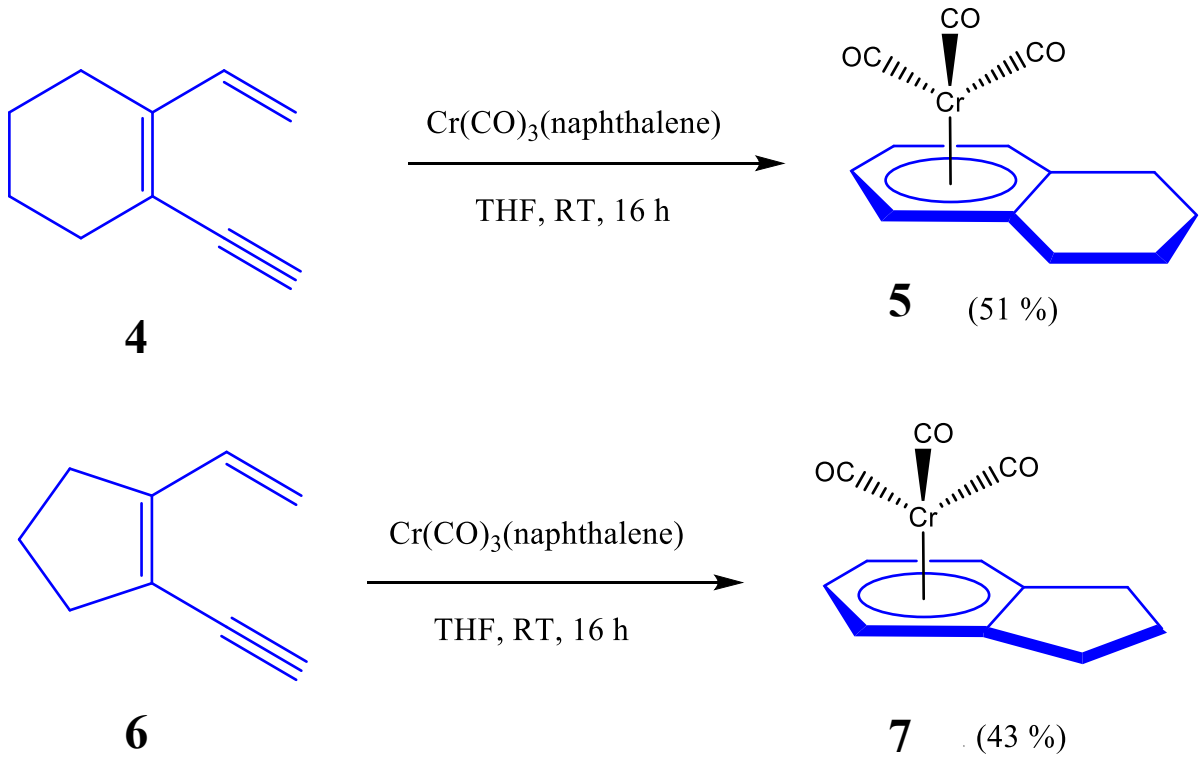

Scheme 1-5: **1** mediated electrocyclization of **4** and **6**

Our study expanded in scope beyond simple dienynes to bulker substrates. Dienyne **8** and **9** were synthesized by performing a methylation on **10** and **11**, respectively. Under the same conditions, arene products **12** and **13** were obtained at a yield of 55 % and 56 %, respectively. Crystallization was successfully performed on **12** and an X-ray crystal structure was obtained (Figure 1-1). The crystal structure in Figure 3-1 indicated the C1-C6 distance (1.421 Å) is identical to the C3-C4 distance (1.417 Å)

which proved the bond formation between C1 and C6. It was also obvious that the bond distances between Cr center to C1, C2, C5 and C6 (2.20 to 2.23 Å) are slightly shorter than the distance between the Cr center to C3 and C4 (2.24 to 2.25 Å). This difference in bond length was likely because the cyclohexane ring caused rigidness of the C3-C4 bond.

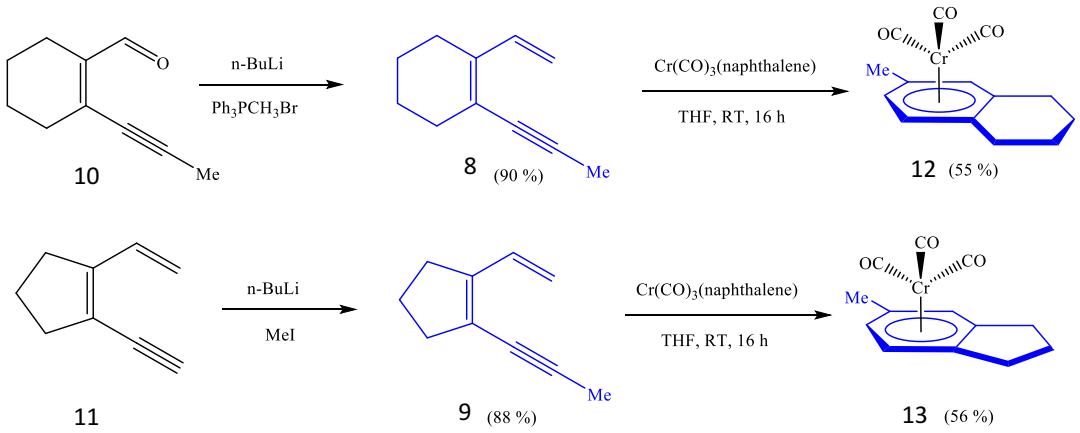

Scheme 1-6: Synthesis of **8,9** and **1** mediated electroscyclization

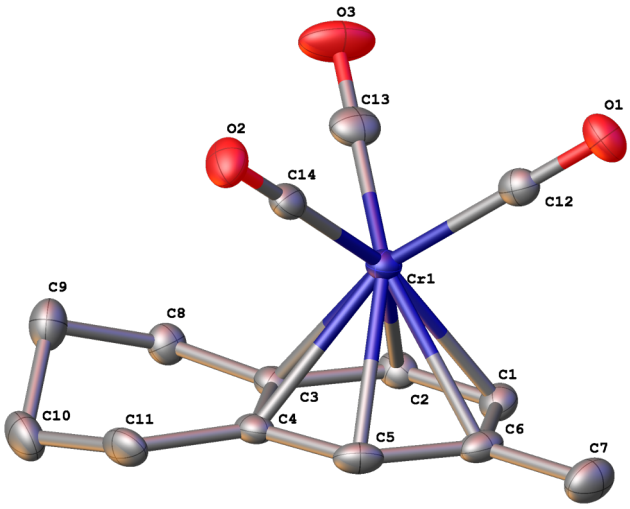

Figure 1-1: X-ray crustal structure of **12**, hydrogens atoms are not shown.

12 could also be synthesized using a different dienyne substrate, **14** by treating it with **1** under similar conditions, but the yield (23 %) was considerably lower. We speculated that the cause of the lower yield was that only one isomer was suitable to produce the cyclization, but we have not yet investigated its mechanism.

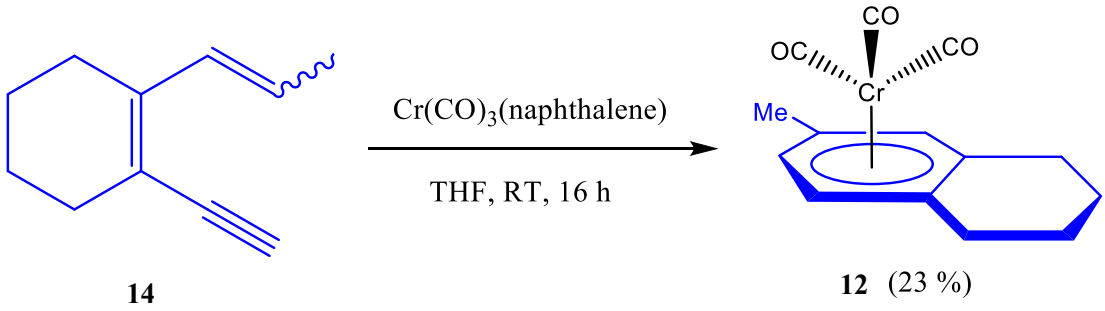

14 **12** (23 %)

Scheme 1-7: **1** mediated electrocyclization of **14**

Cyclization was again successfully achieved for a bulk substituted dienyne **15**. Unfortunately, we were not able to obtain a neat NMR spectrum of the metal coordinated arene product **16** likely due to the multiple arene binding sites available for Cr coordination. However, after exposing it to atmosphere and sunlight for 72 hours, organic arene product **17** was isolated at a 27 % yield.

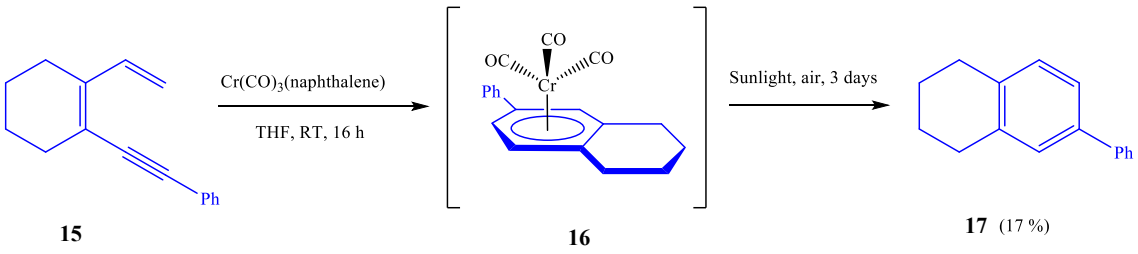

15 **16** **17** (17 %)

Scheme 1-8: **1** mediated electrocyclization of **15**

18 and **19** were not able to produce any arene products. This result was consistent with our previously reported study of reacting **18** and **19** with **1**, in which we believed the steric hindrance of TMS prohibits the formation of the arene product. Unfortunately, the attempts in isolating the possible $(CO)_3Cr(\eta^6$-dienyne) complex were not successful.

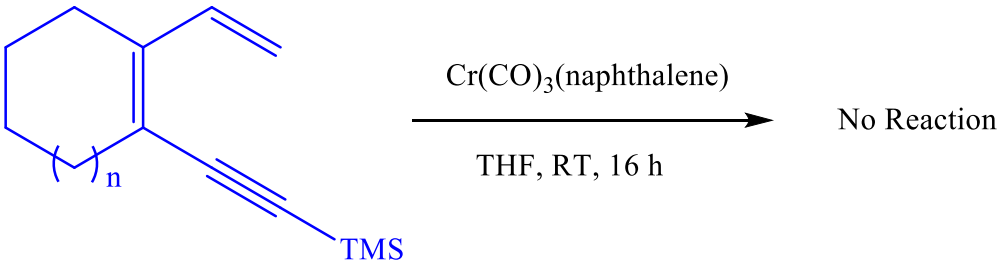

18 n=1
19 n=0

Scheme 1-9: **18** and **19** failed to cyclize when reacting with **1**

Reaction conditions were also examined in non-coordinating solvents such as $CHCl_3$ and CH_2Cl_2. In those solvents, **1** remained in its precursor state without naphthalene dissociation. Heating to 70 °C or exposing the reaction mixture to 252 nm ultraviolet light did not accelerate the cyclization but only resulted in the decomposition of **1**. Only unreacted substrate and free naphthalene were obtained after chromatography.

3. Mechanistic investigation and kinetic study with Fourier-transform infrared spectroscopy (FT-IR).

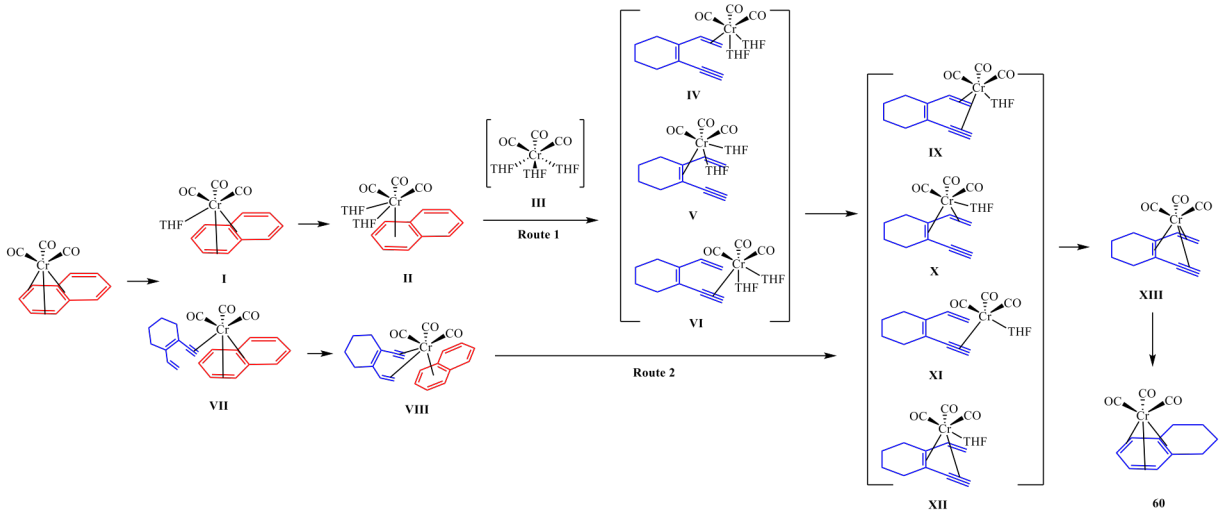

Scheme 1-10: Proposed Mechanism

Scheme 1-1: Proposed mechanism routes and intermediates of Cr-mediated dienyne electrocyclization

We proposed a stepwise naphthalene dissociation and dienyne coordination mechanism during the cyclization and hoped to observe any intermediates via ^{1}H NMR spectroscopy (Scheme 1-10). However, precipitation resulting from minor

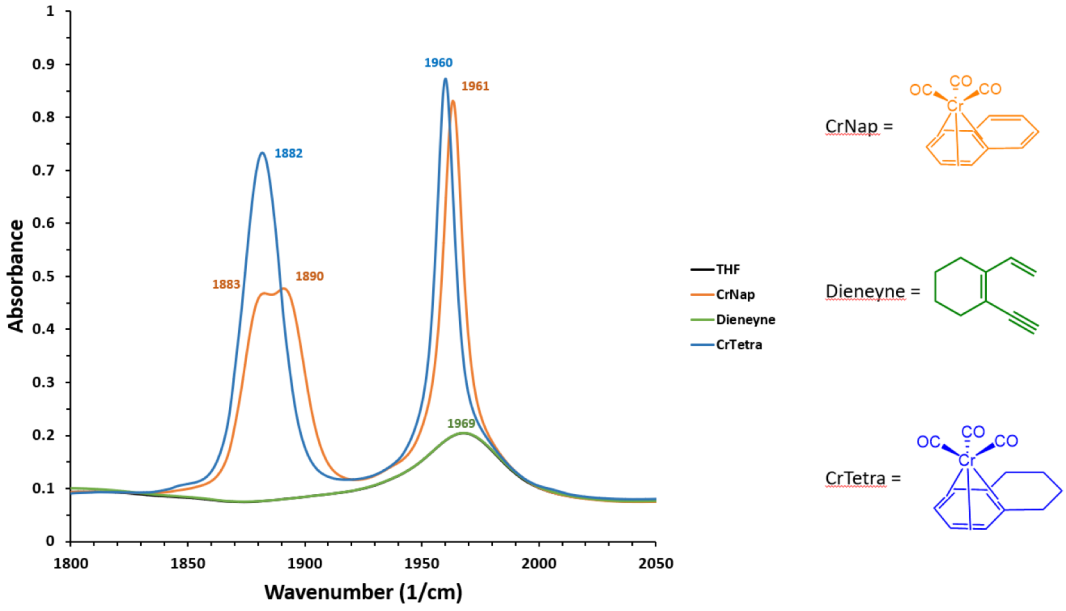

Figure 1-2: FTIR spectrum for isolated reactant and product.

decomposition of the **1** prohibits the convenience of monitoring such reactions with ^{1}H NMR spectroscopy, thus we carried out a mechanistic study with FT-IR spectroscopy by monitoring the change in antisymmetric carbonyl stretching frequency. The IR spectra of **1** *v*(CO): 1883, 1890, 1961 cm^{-1} and **5** *v*(CO): 1882, 1960 cm^{-1} were recorded separately (Figure 3-2). Into an airtight IR cell, was injected 0.1 mL THF solution containing **1** and **4** in a 1: 10 mole ratio mixture. At 23 °C, a dramatic increase in absorption at 1938 cm^{-1} was observed which could be due to a Cr(η^6-enediyne) intermediate (Figure 3-3). After 20 h, the IR absorption at 1938 cm^{-1} decreased with a corresponding increase in an absorption at 1960 cm^{-1} due to the formation of **5**. In addition, we observed a decomposition product with an absorption at 1978 cm^{-1}. To identify the decomposed product, we performed control samples of **4** reacting with **1** in THF under atmosphere (Figure 3-4, blue), **1** solution in THF exposed to ambient air (Figure 3-4, yellow) and a $CrCO_6$ solution in THF (Figure 3-4, red). All three samples had an absorption at 1978 cm^{-1} (Figure 3-4) while such an absorption peak was not

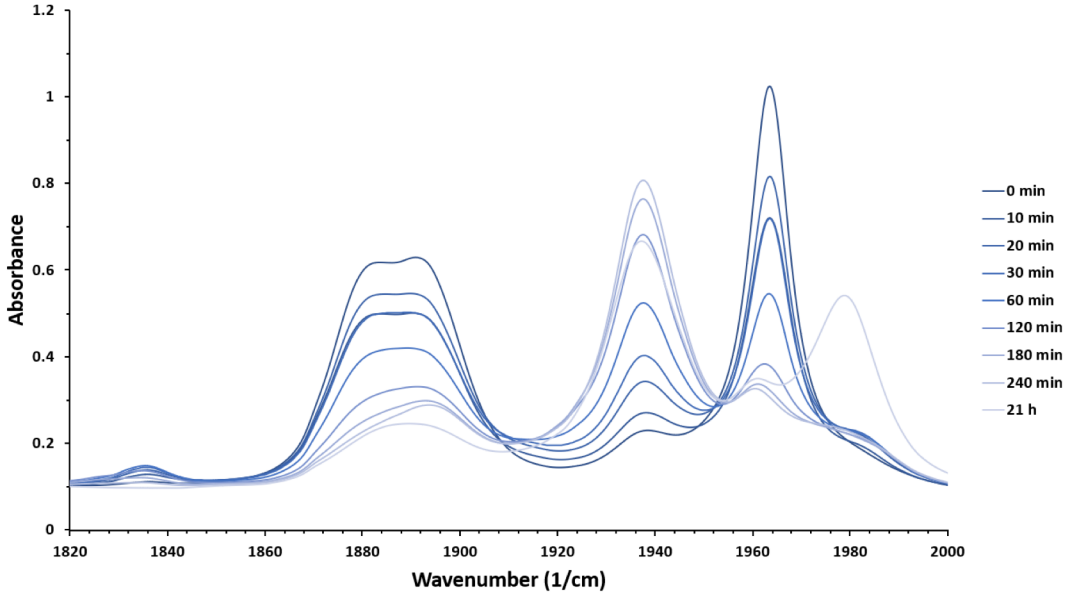

Figure 1-3: FT-IR monitored reaction of **4** with **1** in a 10:1 mole ratio in THF.

observed in the case of the **1** solution sample stored under N_2. The decomposition product exhibited absorptions that are identical to those of $Cr(CO)_6$, which suggests that **1** underwent a highly complex decomposition mechanism in solution when a leakage of air was introduced.

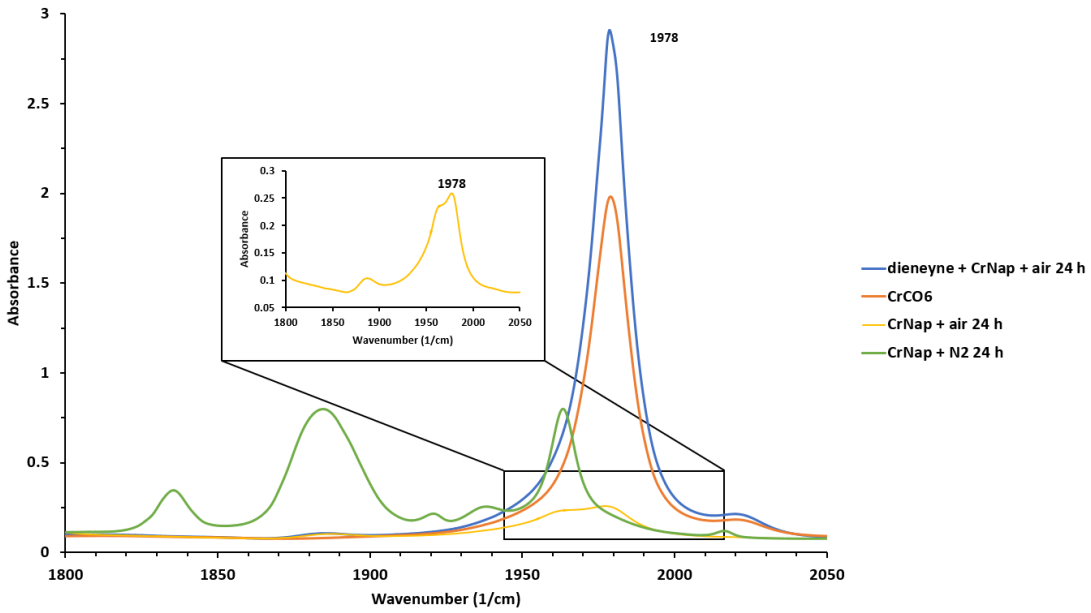

Figure 1-4: FTIR spectrum of **1** under ambient atmosphere (yellow), **1** reacting with **4** under ambient air (blue), **1** under N_2 (green) and $CrCO_6$ (red).

To confirm our hypothesis on the Cr(η^6-enediyne) intermediate as the crucial pathway towards cyclization, we again performed a reaction of **1** and **18** in the IR cell**.** As predicted, an intermediate IR absorption at 1938 cm^{-1} was again observed. After 20 hours, the speculative intermediate peak did not decrease in intensity, this was believed

to be as a result of the failure in forming the cyclized product (Figure 1-5). Thus, the "intermediate" peak remained in this case.

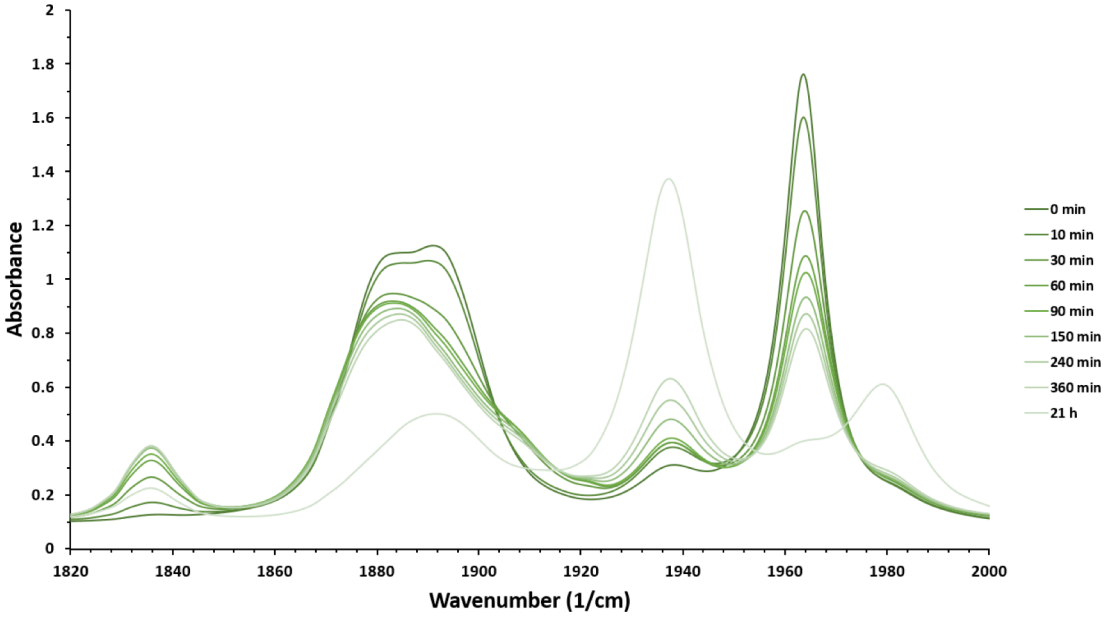

Figure 1-5: FTIR monitored reaction of **18** with **1** in a 10:1 mole ratio in THF.

Solvent influences were studied in the same manner. We believe that the formation of the Cr(η^6-enediyne) intermediate requires that it be performed in a coordination solvent. Thus, a control study in 2,5-dimethyltetrahydrofuran was carried

out with **4**. Within 240 min, the peak intensity of an absorption at 1983 cm^{-1} relative to

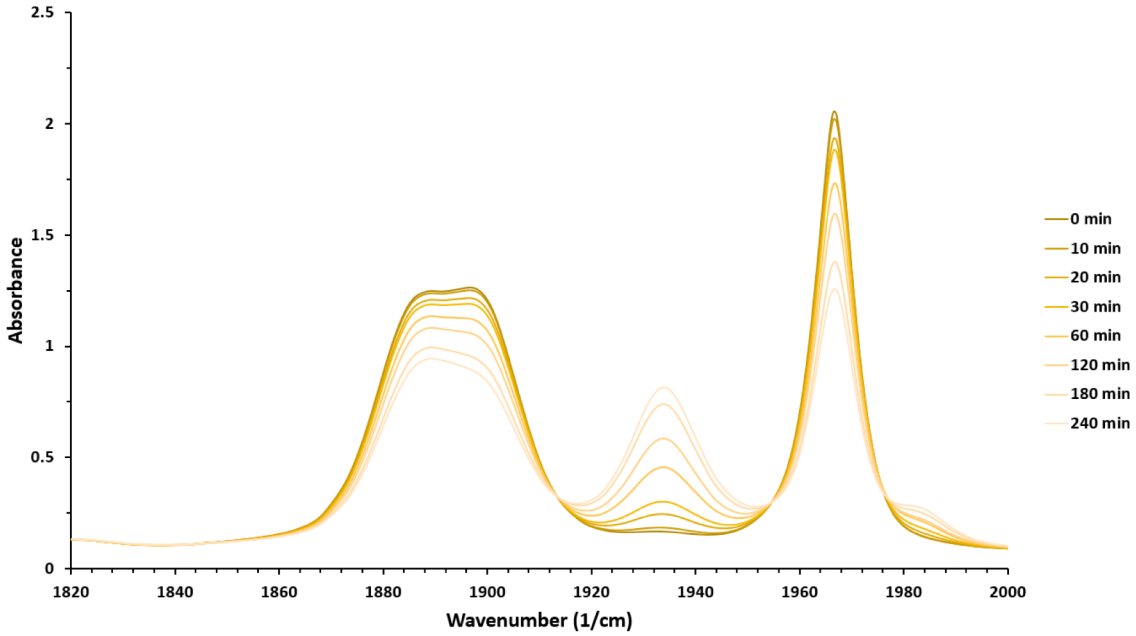

Figure 1-6: FTIR monitored reaction of **4** with **1** in a 10:1 mole ratio in 2,5-dimethyltetrahydrofuran.

the starting material absorption was much lower than the case of the THF solvent, indicating that the intermediate was formed at a much slower rate (Figure 1-6) caused by the steric hindrance of the solvent.[14] The retardation resulting from the bulky coordination solvent suggests that the solvent plays an important role in naphthalene dissociation and substrate re-coordination. Thus, we believe the step wise dissociation presented in route one is likely the major reaction pathway.

Based on the previous experience with **1** mediated dienyne cyclization studies, the bond formation from the hexahepto to the arene product is the rate determining step as determined by calculation. It is reasonable to assume the same result can be applied in this study, in which the slow step should be the step where **XIII** converts into **5**. In another word, the intermediate we observed at 1983 cm^{-1} likely belongs to **XIII**.

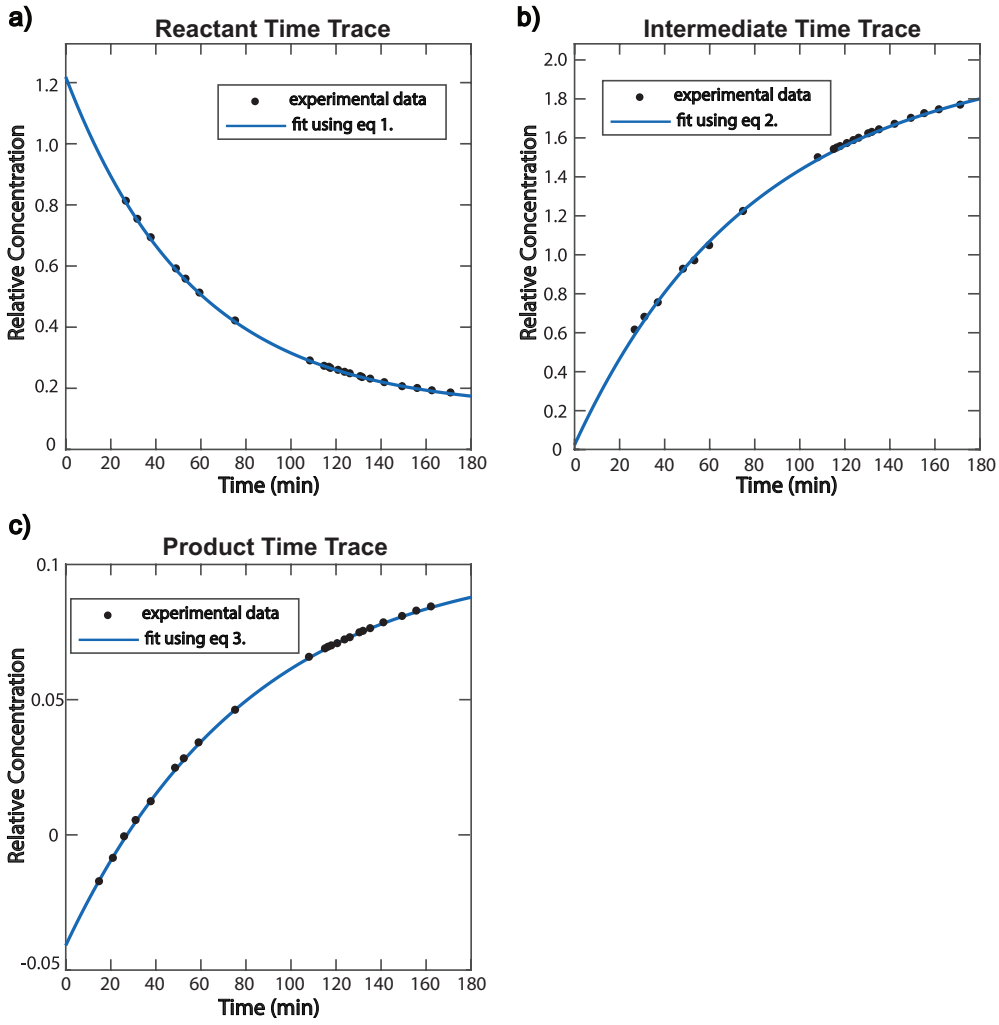

Figure 1-7: Time trace of reactant **1**, intermediate and product **5**. Each component is separated with multivariate analysis for each FTIR spectrum that taken at different time points. Experimental data is then fitted with equation 1,2, and 3, respectively. Reative concentrations of reactant (a), intermediate(b), and product(c) are plotted as a function of time

We were also able to retrieve kinetic information from the FT-IR study. Multivariate regression was applied to extract the reactant, the intermediate and the product time trace from the FT-IR spectrum (Figure 3-7). The model we use to simulate is a two-step, first-order consecutive reaction:[15]

$$R \underset{k_2}{\overset{k_1}{\rightleftharpoons}} \mathrm{I} \xrightarrow{k_2} \mathrm{P}$$

The rate constant can be represented in the following expressions:[15]

$$[R](t) = \frac{[R]_0(\lambda_2 - k_1)}{(\lambda_2 - \lambda_1)}\left(e^{-\lambda_1 t} + Ae^{-\lambda_2 t}\right) \quad (1)$$

$$[I](t) = \frac{[R]_0(k_1)}{(\lambda_2 - \lambda_1)}\left(e^{-\lambda_1 t} - e^{-\lambda_2 t}\right) \quad (2)$$

$$[P](t) = [R]_0 - [R](t) - [I](t), \quad (3)$$

Where the rate constant can be calculated with:[15]

$$k_1 = \frac{A\lambda_2 + \lambda_1}{A+1}\ , k_2 = \frac{\lambda_1 \lambda_2}{k_1}\ , and\ k_{-1} = \lambda_1 + \lambda_2 - k_1 - k_2. \quad (4)$$

Fitting the experimental data to equation 1, 2 and 3 and calculating from equation 4 yields the rate constants to be:

Rate Constant	
$k_1(s^{-1})$	0.0128244
$k_2(s^{-1})$	0.0001183
$k_{-1}(s^{-1})$	0.0015329

In agreement with our expectation, the results indicated that $k_1 + k_{-1} >> k_2$. we observed that the intermediate peak started appearing almost immediately once the reaction starts, indicating that the first step of the reaction took place rapidly. In addition, the fact that the intermediate peak grew gradually after 6 hours and finally decreased after 20 hours supported the assumption that the rate of the second step of the reaction was much slower than the first step. Therefore, the rate constants designate that the cyclization from **XIII** to **5** was more likely to be the rate determining step.

4. 2D-IR in determining intermediates.

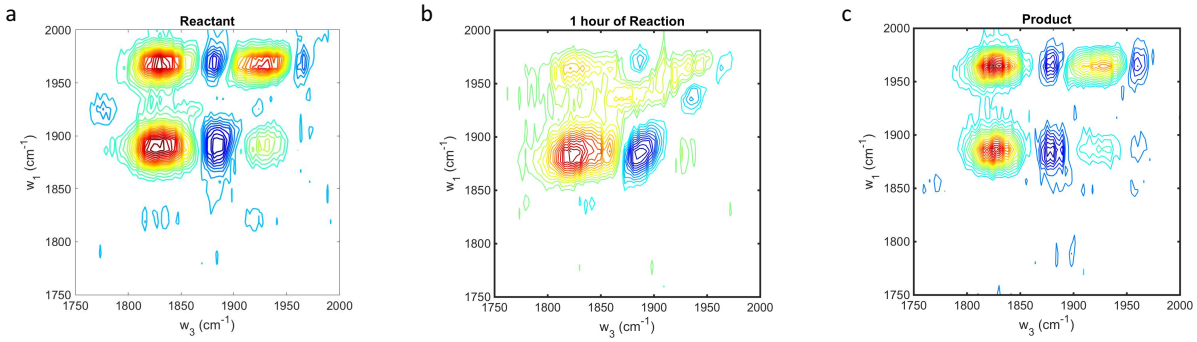

Figure 1-8: 2DIR spectrum of reactant(a), first hour of reaction(b), and product(c)

In order to comprehend the reaction intermediate, we performed 2D-IR experiments. 2D-IR allowed us to differentiate spectral peaks better and thereby distinguish species better. From the reactant 2D-IR spectrum, we observed one pair of peak at ω_1= 1883cm^{-1}, where the peak at diagonal ω_3 = 1883 cm^{-1}, is the v=0$\rightarrow$1 fundamental transition, and the redshifted peak at ω_3 = 1829cm^{-1}, corresponds to the v=1$\rightarrow$2 overtone transition. The fundamental and overtone peaks are separated due to anharmonicity. Another pair of peaks can be seen at ω_1= 1960cm^{-1}. Similarly, we observed peaks at 1882cm^{-1} and 1960cm^{-1} of the products. Both spectra also exhibited cross peaks, indicating the peaks at 1882cm^{-1} and 1960cm^{-1} are coupled to each other. As the reaction continued, we observed that the intermediate vibrational peak and overtone peak features appeared at ω1=1938 cm^{-1} (Figure 1-8c).

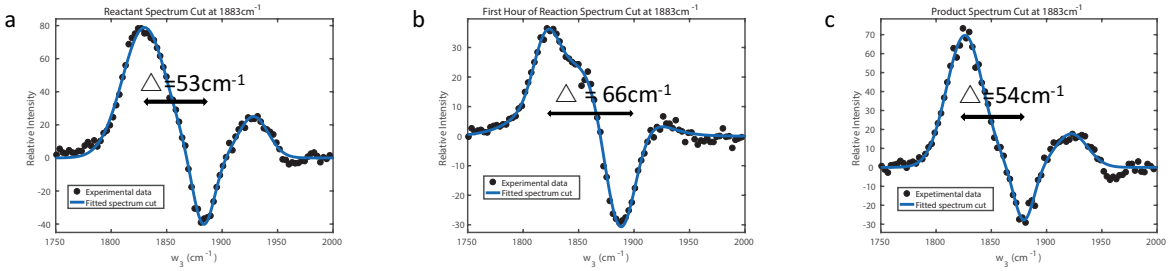

Figure 1-9: 2D-IR spectrum cut at 1883 cm^{-1} fitted with Gaussian function. Intensity as a function of wavenumber. (a) **1** peak's anharmonic shift is 53 cm^{-1}; (b) One hour of reaction peak's anharmonic shift is 66 cm^{-1}; (c) **5** peak's anharmonic shift is 54 cm^{-1}.

Furthermore, 2D-IR allowed the acquisition of the anharmonic shift of molecular vibrations. We retrieved the anharmonic shift by applying a cut at 1883 cm^{-1} and 1960 cm^{-1}. For the reactant and the product, the anharmonic shift is of similar values at 53 cm^{-1} and 54 cm^{-1} at both 1883 cm^{-1} and 1960 cm^{-1}, respectively. However, a 13 cm^{-1} shift in anharmonic shift was observed in the one-hour reaction which could not be distinguished through FT-IR at 1883 cm^{-1} (Figure 1-9) while 1960 cm^{-1} remained unchanged (Figure 1-10). This indicates that this intermediate vibrational peak overlapped with the reactant and product absorption peaks at 1883 cm^{-1}. With 2D-IR, the intermediate vibrational peak's position was further revealed.

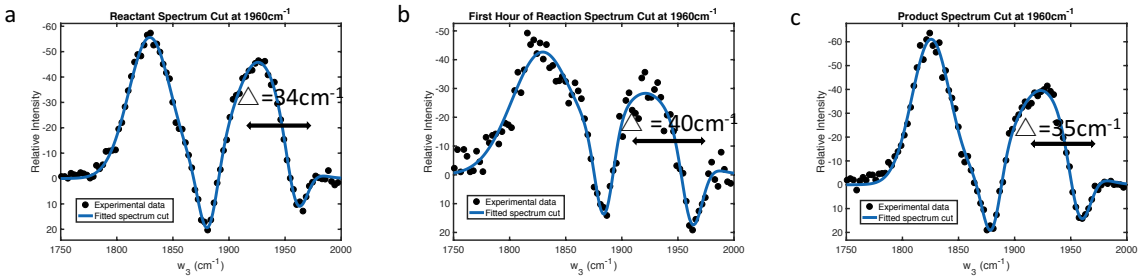

Figure 1-10: 2D-IR spectrum cut at 1960 cm^{-1} fitted with Gaussian function. Intensity as a function of wavenumber. (a) **1** peak's anharmonic shift is 34 cm^{-1}; (b) One hour of reaction peak's anharmonic shift is 40 cm^{-1}; (c) **5** peak's anharmonic shift is 35 cm^{-1}.

Our observation was supported by our collaborator Prof. Baldridge's computational study. The structure of **XIII** was stablished via the BP86 density function with an ultrafine grid, together with the Def2-TZVPP basis set (Table 3-1). The antisymmetric *v*(CO) vibrational stretching frequencies were calculated to be 1833.6 and 1859.0 cm^{-1}, the symmetric stretches in combination with the interacting triple bond stretch were calculated to be 1934.5 cm^{-1} and 1997.5 cm^{-1}. The absorbance at 1833.6 cm^{-1} and 1934.5 cm^{-1} can be directly observed from the FT-IR spectrum (Figure 1-3). The antisymmetric stretch absorbance at 1859 cm^{-1} was not directly obtained from the IR spectrum but a negative peak shoulder at ~1855 cm^{-1} was observed and believed to be an overtone peak from the 1859 cm^{-1} absorbance peak. Although we speculate an absorbance peak was exhibited at ~1997 cm^{-1} (Figure 1-9b), it was not confirmed due to its low intensity relative to noise. Combining the results obtained from the IR study and the computation, it is reasonable to believe the intermediate we observed very likely to be **XIII.**

5. Proposed Mechanism.

With the evidence given by IR studies and the model given by previous studies with [Cp*Ru(η^6-dienyne)]PF_6, we speculate the mechanism shown in scheme 3-10 as the most probable reaction pathway. The coordination solvent promotes the dissociation of naphthalene from **1** to generate $Cr(CO)_3L_3$. A fast equilibrium is then established between $Cr(CO)_3L_3$ and the $Cr(CO)_3$(η^6-dienyne) intermediate, which is believed to be the contributor of the intermediate peak observed in IR at 1938 cm^{-1}. The formation of the product may undergo two pathways, a [1,3] hydride shift or a [1,2] hydride shift, as suggested by the previous O'Connor cyclization reported by our group.

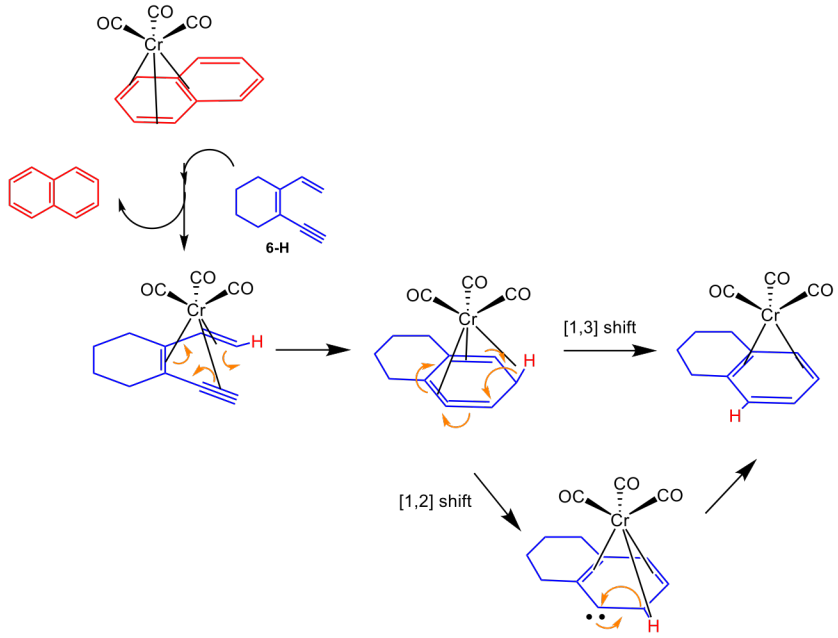

Figure 1-11: Speculative mechanism of **1** mediated dienyne cyclization.

6. Conclusions and Future work.

Here we report that an oxygen and moisture stable complex $Cr(CO)_3(\eta^6$-naphthalene) promotes the dienyne cyclization under ambient temperature in moderate yield; thereby demonstrating that the prior observation of the ruthenium-mediated cyclization may also work with other metals. Bulky coordinating solvents and bulky alkyne substituents, such as TMS, prohibited the cyclization due to the steric hindrance which matches what we observed in the previous ruthenium study. The IR spectroscopic studies provided evidence for the formation the observable intermediate. We speculate it to be the $Cr(CO)_3(\eta^6$-dienyne) intermediate based on the previously reported ruthenium-mediated dienyne cyclization. However, the information we obtained from the 2D-IR studies did not give a concrete identification of the intermediate. We are currently conducting calculations in order to verify the best explanation for the complex that was observed in IR studies.

7. Experimental.

7.1 General procedures

Standard Schlenk technique or a nitrogen-filled glovebox are applied in all NMR reactions between dienyne substrates and metal complexes. Flash column chromatographic purifications were performed using silica gal (60 Å, particle size 43-60 um, 230-400 mesh, EMD Chemicals). ^{1}H and ^{13}C NMR spectra were recorded on Varian Mercury 400 MHz or Varian VX 500 MHz instruments. ^{1}H and ^{13}C NMR chemical shifts (δ) are reported in parts per million (ppm). Spectra were referenced to the residual solvent peak. Chloroform was dried by refluxing with CaH_2 overnight and THF was dried over activated molecular sieves followed by distillation under static vacuum. The structural and energetic analyses of the molecular systems described in this study were carried out using the BP86 density functional, with an ultrafine grid, together with the Def2-TZVPP basis set. Effects of solvent were included by the continuum solvation model based the original COSMO theory of Klamt modified for *ab initio* theory, with a dielectric for THF. Full geometry optimizations were performed and uniquely characterized via second derivative (Hessian) analysis to establish stationary points and effects of zero-point energy and thermal corrections. Visualization and analysis of structural was carried out using Avogadro and WebMO.

7.2 FT-IR and 2D-IR.

To monitor the reaction, 0.1 mL reaction mixture was injected into an airtight IR flow cell equipped with Teflon caps and infrared spectra were obtained on a Nicolet iS10 FT-IR. High/low resolution mass spectra analyses were performed at the mass spectrometer facility at UC San Diego. Two-dimensional infrared (2D IR) spectroscopy is applied to investigate the mechanism of the reaction. The setup scheme is shown in Figure 3-10. 800-nm laser pulses (~35 fs, ~5 W, 1 kHz) generated by an ultrafast Ti:Sapphire regenerative amplifier (Astrella, Coherent) are sent into an optical parametric amplifier (OPA) (TOPAS, LightConversion) which outputs tunable near-IR pulses. The near-IR pulses are converted to mid-IR pulses through a difference frequency generation (DFG) process by a type II $AgGaS_2$ crystal (Eksma). After DFG, a CaF_2 wedge splits the mid-IR pulse into two parts: the 95 % transmitted part is sent into a Ge-Acoustic Optical Modulator based mid IR pulse shaper (QuickShape, PhaseTech) and is shaped to double pulses, which forms the pump beam arm; the 5 % reflected is the probe beam. Both pump (~ 1.1 μJ) and probe (~ 0.2 μJ) are focused by a parabolic mirror (f = 10 cm) and overlap spatially at the sample. The output signal is collimated by another parabolic mirror (f = 10 cm) at a symmetric position. The pulse sequence is shown in Figure 3-12. Two pump pulses and a probe pulse (pulse duration of 100~150 fs) interact with samples at delayed times (t_1, t_2 and t_3). After the first IR pulse, a

vibrational coherence is generated, which is converted into a subsequent state by the second IR pulse and is characterized by scanning t_1 (0 to 4000 fs with 20 fs steps) using the mid IR pulse shaper. A rotating frame at f_0 = 1583 cm^{-1} is applied to shift the oscillation period to 80 fs and to make the scanning step meet the Nyquist frequency

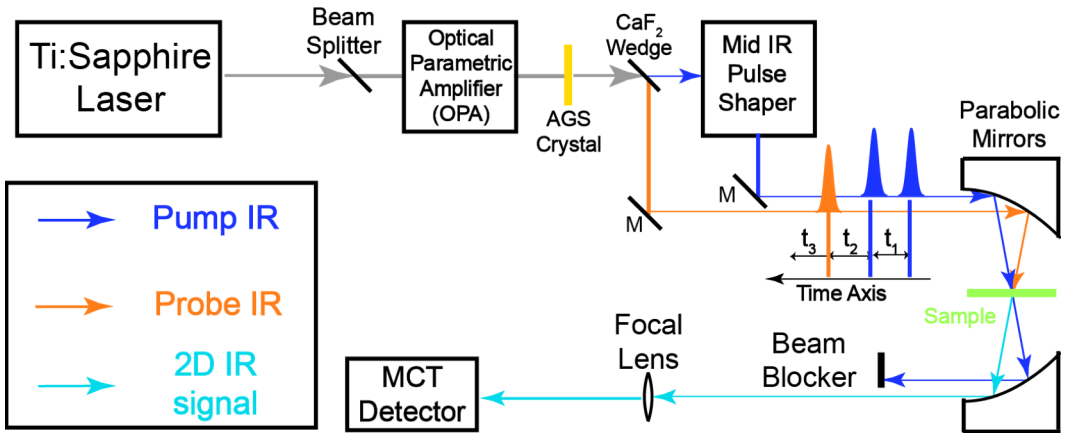

Figure 1-12: Scheme of the 2D-IR setup in this study.

requirement. After waiting for t_2, the third IR pulse (probe) is impinged on the sample, and the resulting macroscopic polarization emits an IR signal. The monochromator and MCT (Mercury-Cadmium-Telluride) IR (infrared) Detector (PhaseTech) experimentally Fourier transform the signal, thus generating a spectrum along the ω_3 axis. Numerical Fourier transform of the signal along the t_1 axis is required to obtain the spectrum along ω_1. The resulting 2D-IR spectra are plotted against ω_1 and ω_3. The t_2 time delay is controlled by a computerized delay stage and fixed at 500 fs. The whole data collection process is done by home-written LabVIEW programs. 2D-IR spectra were obtained at designated markers in the timelines to characterize the kinetics of the chemical reaction.

8. Acknowledgments.

The material in Chapter 1, is currently under preparation for publication with the following authors.: Chen, Liying*; Steger, Han*, Baldridge, Kim K.; Xiong, Wei; O'Connor, Joseph M. The thesis author was the primary investigator and author of this material.

9. References.

1. Hopf, H.; Musso, H. Angew. *Chem. Int. Ed. Engl*. **1969**, 8, 680. “Preparation of Benzene by Pyrolysis of cis-and trans-1,3-Hexadien-5-yne”.

2. Bergman, R.G. *Acc. Chem. Res.* **1973**, *6*, 25-31. “Reactive 1.4-Dehydroaromatics”.

3. Mandal, S.; Basak. *Tetrahedron Letters*. **2009**, 50, 3641-3644. “Aza Hopf cyclization: synthesis and reactivity of cyclic azadieneynes”.

4. Wan, Y.; Zheng, X.; Ma, C. *Angew. Chem*. **2018**, 130, 5580-5584. “Conjugated Dienyne-Imides as Robust Precursors of 1-Azatrienes for 6 pi Electroncyclizations to Furo[2,3-b]dihydripyridine cores”.

5. Capitani, J. F.; Gaffney, S. M.; Castaldo, L.; Mitra, A. *Current Topics in Medicinal Chemistry*. **2008**, 8, 470-486. “The Critizal Distance of the Cycloaromatization Reactions of Enediynes”.

6. O’Connor, J. M.; Friese, S. J.; Tichenor, M. *J. Am. Chem. Soc*. **2002**, 124, 3506-3507. “Ruthenium-Mediated Cycloaromatization of Acyclic Enediynes and Dienynes at Ambient Temperature”.

7. O‘Connor, J. M.; Friese, S. J.; Rodgers, B. L.; Rheingold, A. L.; Zakharov, L. *J. Am. Chem. Soc.* **2005**, 127, 9346-9347. “An η^6-Dienyne Transition-Metal Complex”.

8. Hitt, D. M.; O’Connor, J. M. *Chem. Rev*. **2011**, 111, 7904-7922. “Acceleration of Conjugated Dinyne Cycloaromatization”.

9. Bland, W. J.; Davis, R.; Durrant, J. L. A. *J. Organometallic. Chem*. **1985**, 280, 95-103. “The mechanism of the addition of haloalkanes to alkenes in the presence of tricarbonyl-η^6-naphthalenechromium(0), [$Cr(CO)_3(\eta^6\text{-}C_{10}H_8)$]”.

10. Blagg, J.; Davies, S. G.; Goodfellow, C. L.; Sutton, K. H. *J. Chem. Soc. Perkin Trans.* **1990**, 1, 1133-1144. “Regioselective nucleophilic additions to tricarbonyl(η^6-arene)chromium(0) complexes: electronic *versus* chelation control”.

11. Blagg, J.; Davies, S. G.; Goodfwllow, C. L.; Sutten, H. H. *J. Chem. Soc. Perkin Trans.* **1987.** 1805-1811. “The Diastereoselective Functionalisation of Arene Tricarbonylchromium Complexes Containing a Benzylic Heteroatom Substituent”.

12. Ylijoki, K. E. O.; Lavy, S.; Fretzen, A.; Kundig, P. E.; Berclaz, T.; Bernardinelli, G.; Besnard, C. *Organometallics.* **2012**, 31, 5396-5404. “A Synthetic and Mechanistic Investigation of the Chromium Tricarbonyl-Mediated Masamune–Bergman Cyclization. Direct Observation of a Ground-State Triplet *p*-Benzyne Biradical”.

13. Qin, P.; Cope, S.; Steger, H.; Veccharelli, K. M..; Holland, R. L.; Hitt, D. M.; Moore, C. E.‘ Baldridge, K. K.; O’Connor, J. M. *Organometallic*. **2017**, 36, 3967-3973. “Photoactivated Transition-Metal Triggers for Ambient Temperature Enediyne and Dienyne Cyclization: Rutenium-η^6 -Naphthalene Complexes”.

14. Wax, M. J.; Bergman, R. G. *J. Am. Chem. Soc.* **1981**, 103, 7028-7030. “Direct Evidence for Solvent Coordination in Migratory CO Insertion”.

15. Ramachandran, B. R., Halpern, A. M. *J. Chem. Ed.* **1997**, 74, 975-978. “A Novel Experiment in Chemical Kinetics: The A→ B → C Reaction System

Chapter 2 Strain-induced ferroelectricity in metal halide perovskites

1.Abstract

Metal halide perovskites have shown plenty of extraordinary optoelectronic properties, making them good candidates in various applications[1-4]. Specifically, ferroelectricity is considered as the possible origin in achieving such excellent photovoltaic performance and high-power conversion efficiency[5,6]. However, whether halide perovskites, especially those with polar molecules at A site, have strong and stable ferroelectricity is still debatable. Previous researchers have studied polar molecule or atom displacement induced ferroelectricity in halide perovskites like methylammonium lead iodide ($MAPbI_3$)[7-13]. Many other studies also show that such polarity originates from the measurement artifacts, and $MAPbI_3$ is ferroelastic[14-18]. While the presence of persistent ferroelectricity in a large domain of the freestanding $MAPbI_3$ is still controversial[1,12,19], we found that the epitaxial strain can serve as an effective tool to create ferroelectricity in the epitaxial metal halide perovskites. Here, we investigate the ferroelectricity in the freestanding $MAPbI_3$ material that is ferroelastic rather than ferroelectric. In the meantime, we apply strain engineering to tetragonal α-formamidinium lead iodide (α-$FAPbI_3$) using both theoretical simulations and experimental techniques. Through tailoring the bulk perovskite substrate, the epitaxial α-$FAPbI_3$ is applied with a compressive strain up to 2.4 percent[20]. By thermally stimulated depolarization current (TSDC) measurement, the polarization of the epitaxial strain α-$FAPbI_3$ thin film is demonstrated. Through multiple characterization methods, we demonstrate that the ferroelectricity generated in the strained α-$FAPbI_3$ owes to the inorganic framework atom displacement generated from the lead-iodide bonds with neglectable influence of freely-rotational FA^+ molecules under room temperature.

2. Introduction

Ferroelectricity largely enhances the photovoltaic performance and power conversion efficiency in semiconductors due to the enhanced charge separations, carrier lifetimes, and the transcend of Shockley-Queisser limit, etc.[5,6,8,9,21,22]. Moreover, plenty of phenomena like exceeding open circuit bandgap voltage, current-voltage hysteresis, etc., are tightly correlated to the ferroelectricity of the dielectric materia[8,23,24]. Previously, “hard” and “soft” ferroelectricity are discovered with the differences of material defects, coercive field, and the bias field generated through domain defects centers ordering[25]. Single crystalline Halide Perovskite with large and integrate grains is considered as one representative among the soft semiconductors. To determine whether a dielectric semiconductor has ferroelectricity, several factors are critical to declare: (1) the material is lack of inversion symmetry; (2) a spontaneous polarization formation during the paraelectric-to-ferroelectric phase transition; (3) polar domain reorientation under application of high electric field or input voltage[1,7,9]. However, whether freestanding metal halide perovskites possess ferroelectricity remains controversial. Some researchers even attribute the ferroelectric phenomena as the outcome of ferroelasticity instead[1,12,19,26-28]. Shunning from the debate of free-standing halide perovskite, we lay our emphasis on strained halide perovskite. Through applying strains, materials not limited to halide perovskites are able to discover novel properties. Here, the applied strain emerged by epitaxial growth lattice mismatch is able to trigger various compelling phenomena inside perovskite like strain-induced ferroelectricity.

3. Strained α-$FAPbI_3$ Single Crystalline Layer Structure

The α-$FAPbI_3$ single crystalline layer is heteroepitaxially grown on the substrate of mixed methylammonium lead chloride/bromide ($MAPbCl_xBr_{3-x}$) through the inverse temperature growth (ITC) method[20]. With the increase of Cl^-/Br^- ratio from 0 to 1, the lattice mismatch between the epitaxial layer and single-crystal substrate enhances, leading to a growing applied strain to the α-$FAPbI_3$ layer. Additionally, a uniform and consistent strain is discovered under sub-100 nm films with -2.4% strain for 1:1 Cl:Br ratio. The epitaxial layer thickness is limited to 2 microns where the strain of misfit is relaxed at the surface as above[20].

The phase crystallographies of the α-$FAPbI_3$ epitaxial layer in in-plane and out-of-plane directions are illustrated through the high-resolution XRD pattern shown in Fig. 1a. A proportional relationship is discovered between the ratio of chloride in the substrate with the applied strain to the surface. In the freestanding case, both out-of-plane and in-plane directions α-$FAPbI_3$ demonstrates a cubic crystal structure. As the increment of in-plane lattice mismatch, the in-plane compressive strain matches the out-of-plane tensile strain, showing an increasing tetragonality of the α-$FAPbI_3$ lattice. Similar to $MAPbI_3$, the cubic-tetragonal phase transition largely raised the possibility of ferroelectricity in the strained α-$FAPbI_3$ epitaxial layer[2,29]. Under fixed incident x-ray beam angle, the projection intensity ratio decreased as the perovskite tetragonality increase. The angle between (110) and (101) facets tends to increase under cubic-tetragonal phase transition (shown in Fig. 1b). The 45^o and 90^o are stretched when the c-direction of the primitive unit cell extends from cubic structure to tetragonal. A clear

enhancement in pole figure intensity angel-relaxation exhibits in Fig. 1c indicates the tetragonality nature of epitaxial film structure under applied strain based on hetero-lattice mismatch. The agreement between simulation data and the 45^{o}- 46^{o} projection pole figure further demonstrates the strained thin film has undergone a tetragonal phase transition.

Fig 1

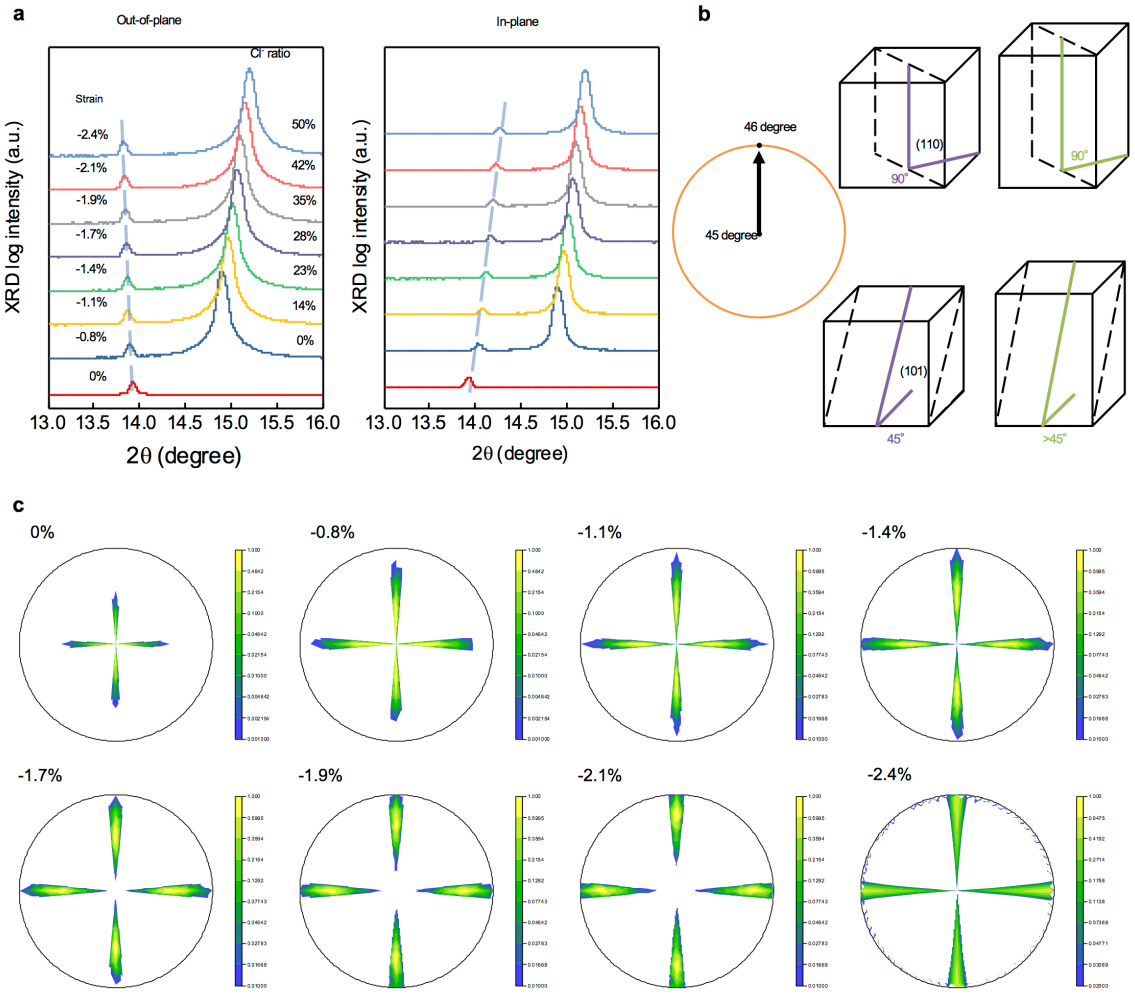

Fig. 1. Strained α-$FAPbI_3$ Structural Characterization a, High-resolution XRD pattern under out-of-plane and in-plane direction. **b**, Pole Figure mechanism in projecting 45° to 46° with cubic phase to tetragonal phase. **c**, Pole Figure detection under freestanding case to -2.4% strain.

4. **Ferroelectricity in α-$FAPbI_3$**

The ferroelectric properties of strained α-$FAPbI_3$ epitaxial layer polarization domain is characterized through Piezoresponse Force Microscopy (PFM). However, regardless of the observed ferroelectricity generated from α-$FAPbI_3$, the debate regarding whether other metal halide perovskite like bulk $MAPbI_3$ is ferroelectric or ferroelastic starts in 2015 and remains controversial, as mentioned above. Different conclusions are also drawn from the same material and the same setup. Single crystalline bulk $MAPbI_3$ has a structural phase transition from cubic to tetragonal at around 315 K[30]. The crystal structure may fluctuate at room temperature (RT) since the phase transition is close to RT, resulting in measurement difficulty. Besides, the ion migration in halide perovskites under a strong electric field can also lead to artifacts during the PFM or hysteresis loop measurement. Hence, to solve these measurement-related problems, Thermally Stimulated Depolarization Current (TSDC) is carried out. TSDC measures the current from the relaxation of the aligned dipole during the temperature increment process. The merit of this measurement is that it can be used to distinguish the difference between the ferro-para phase transition and the non-polar normal phase transition. Specifically, a ferro-para transition is polarized-field-dependent, while a non-polar phase transition is field-independent. Besides, a different magnitude of the electric field can be applied to study and avoid ion migration, which can differentiate the artifact of polarization in halide perovskites. Thus, TSDC measurements are carried out to test the ferroelectric properties based on α-$FAPbI_3$ epitaxial layer and freestanding $MAPbI_3$ single crystals.

During the TSDC measurement, the device is first kept at a bias condition (poling) during the cooling process so that the dipoles are aligned by the external bias. This

process is followed by a heating process without external bias during which the aligned dipoles will start to relax near the curie temperature (T_c), generating a thermally stimulated depolarization current. The magnitude of the depolarization current of a ferroelectric material is linearly proportional to the external electric field during the cooling process within a reasonable voltage so that the ion migration is negligible. Otherwise, ion migration will be trigged by the large electric field so that the magnitude of the measured current will increase dramatically. It is also worth mentioning that non-polar phase transition will also trigger a thermally stimulated current due to the change of atom position while the current being field-independent. This mechanism helps to identify whether one phase transition is polar or not.

We firstly carry out the TSDC measurement on the freestanding as-grown α-$FAPbI_3$ crystal, whose result is shown in Fig. 2a. Increasing temperature is applied to the whole perovskite structure, including the substrate perovskite and epi-layer. A well-distinguished peak is evident, corresponding to the non-polar tetragonal-cubic phase transition under free-standing case shown on the top bar of Fig. 2a. Epitaxially strained α-$FAPbI_3$ thin films under different strain levels (0 to 2.4%) are then measured. Two peaks are observed to show up under 200K and 350K representing the phase transformation corresponding to the perovskite substrate and epitaxial layer correspondingly. From the strain-dependent TSDC measurement results, the peak position of the epitaxial film shifts to the lower temperature with the increasing strain level, while the peak position of the substrate shifts to the higher temperature with the increasing Cl^- content. This temperature change is considered as the result of the increment in temperature difference. While increasing the strain applied by the lattice mismatch between the

epitaxial layer and freestanding substrate, the corresponding lattice displacement is also elevated, resulting in absorbing more temperature to change back to centrosymmetric structures.

Field-dependent TSDC measurement (shown in Fig. 2b) is then carried out to verify the epitaxially strained samples. The peak intensity and position are further extracted to plot as a function of the applied bias voltage, as shown in Fig. 2c. The applied electrical field shows a variance between the epitaxial layer signal against the substrate signal. Increasing temperature leads to the polarization relaxation direction changes accompanied by the generation of pyroelectric current. At the relatively low applied external voltage, the peak intensity of the TSDC from the epitaxial thin film increases linearly while the peak position remains unchanged, representing that the TSDC peak results from the ferro-para transition in the epitaxial thin film. Further increasing the voltage provides enough activation energy for ion migration and leads to severe ion migration, as well as structural damage, during the poling process.

In the following heating stage, the migrated ions recover under the built-in electric field, which increases the peak intensity dramatically. Meanwhile, the peak position also changes due to the structural damage induced by the ion migration. On the contrary, the peak intensity of the TSDC from the substrate phase transition barely varies, demonstrating the non-polar nature. Therefore, we have successfully shown that the ferroelectricity in the epitaxially strained α-$FAPbI_3$ thin films, which is absent in their free-standing counterpart.

Need to point out, the extension temperature range of peak signals under 40V bias for both substrate material and the epitaxial layer is due to the enhancement of

background noise under the fact of a high applied field. Again, the peak positions and intensities in Fig. 2b are extracted and shown mathematically in Fig. 2c. As calibrated, the ferroelectric peak intensity is positively proportional to the applied field (voltage applied). However, when approaching the voltage threshold (above 30V), the ferroelectricity in perovskite turns into non-ferroelectricity due to the ion migrations and permanent sample damage induced by the extreme voltage applied that vanishes the percent strain in the epitaxial layer. Hence, both peak position against temperature and stimulated current shift off from the linear calibration curve.

Fig 2

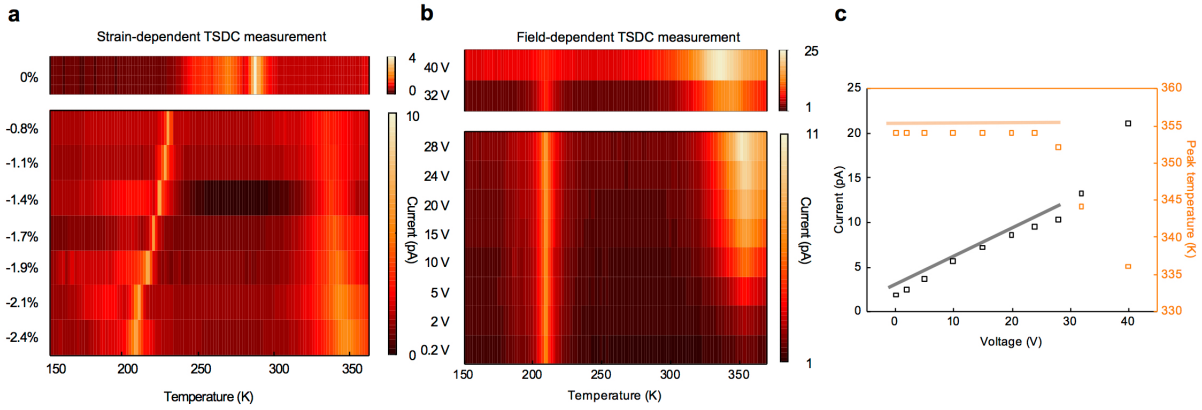

Fig. 2. TSDC measurement **a**, Strain-dependent TSDC Measurement with two peaks shows up representing mixed halide group perovskite substrate and strained epitaxial layer. **b**, Field-dependent TSDC measurements with no peak change representing field-independent Perovskite substrate. **c**, Calibrated peak intensity correspond to increasing applied voltage against Current and temperature. Tendency is calibrated and shown with line. Peak intensity shifts off above 30V.

5. Strain-induced Ferroelectricity Origin

The molecular origin of the strain-induced ferroelectricity is examined in the halide perovskite structure. It is widely believed that the strain tends to induce the change in cation rotations within the perovskite molecule frameworks or deform the bond strength and angles based on the inorganic framework. To clarify whether the ferro-center sources from the organic part or not (in this case, the FA^+ cation), the trainsient IR absorption measurement is carried out.

Fig. 3a displays the data acquired in parallel and perpendicular polaritzation configurations between the pump and probe pulses (Ipara and Iperp, respectively). The spectra are dominated by two features. The negative feature centered at 1726 cm^{-1} corresponds to ground state bleach (GSB) and stimulated emission (SE) signals associated with the 0-1 C−N antisymmetric stretch transition of the FA^+ cation. The positive feature centered at 1714 cm^{-1} is the corresponding excited state 1-2 absorption (ESA) signal. Fig. 3b shows the molecular dynamic using parallel pump probe polarization for a 2.1% force constrain α-$FaPbI_3$ film, which contains both population relaxation and reorientation dynamics. When the polarized pump pulse first excites the molecule, the molecule has a cosine square dependent distribution of excited vibrations; that is, more are excited with their transition dipole vectors along the pump than perpendicular to it. As time goes on, the pump probe signal changes due to the orientationally motions[31], i.e. originally excited transition dipole parallel to the pump pulse, reorient to non-parallel orientations, which results in a smaller pump probe signal if the probe pulse is parallel to the pump.

To quantify rotational dynamics, the anisotropy dynamics of the signal were extracted. To extract the anisotropy decay originating from the C-N asymmetry mode reorientation, we focus on the responses in the center of the GSB/ES feature centered at 1714cm^{-1} because of a better signal-to-noise ratio. The anisotropic response is calculated follows the equation below:

$$R(t) = \frac{I_{para} - I_{perp}}{I_{para} + 2I_{perp}} \quad \text{(Eq. 1)}$$

Fig. 3c shows the extracted anisotropy decay for the strain-free and 2.1% strain α-FAPbI3 film. The initial anisotropies of both systems are close to 0.4, suggesting a random distribution of uncoupled dipoles[32]. Then, the anisotropy decays in a time frame of a few picoseconds. The extracted anisotropy decays are fitted into an exponential decay with an offset. Here we add an offset into the exponential decay since previous studies deduce the long-time offset values for R(t) due to a small portion of cation population is unable to reorient, such as cations at the edge of the lattice[33]. The fitting results gives 0.51 ± 0.02 ps and 1.05 ± 0.04 ps lifetime for strain-free cases and 2.1% strain cases, respectively. Thus, the rotational relaxation of FA cation in strain system is around twice of that of the strain-free systems. We note that the extracted anisotropy decays could also be fitted to two exponential decay (Supplementary Fig. 1) and could be explained using a wobbling in a cone model. However, single exponential function fitted the result well (R^2 > 0.947) in this study.

These observations agree with the Car-Parrinello molecular dynamics (CPMD) simulations in Fig. 3d. We further extract the vector autocorrelation function c(t) of the FA cations defined by the two nitrogen atoms of the FA cation, which relates to the change

in FA reorientation dynamics and reflects the rate at which FA cations rotationally relax inside the PB/I cage. Shown in Fig. 3d, c(t) indicates that the autocorrelation decay is slightly slower when the strain is applied compared to that of the strain-free structure, which is comparable with the experimentally applied compression (2.1%).

To comprehensively understand the relationship between the in-plane compression along with the a and b directions and reorientation lifetime, we check the anisotropy dynamics under different force constrain (Fig. 3e). Fig. 3e indicates that there is a positive correlation between force strain and reorientation lifetime. As previously shown in Fig. 1a, as the in-plane strain increases, the substrate reduces the Pb-I distance along the in-plane directions (a and b axis) and increases the Pb-I distance along the out-plane directions (c axis). This means that the rotational dynamics of the FA cations are hindered by the in-plane strain in compressed inorganic PbI_6 frameworks. Specifically, simulations indicate that the in-plane strain caused by the substrate reduces the Pb-I distances along these in-plane directions; consequently, the bond-length contraction confines the FA cations, restricting their rotational degrees of freedom within the PbI_6 frameworks and limits the octahedral tilting. Furthermore, the experimentally applied compression will reduce the total volume of Pb-I cage, which will restrict rotational motion that leads to a more favorable ordering of the FA cations in the compressed α-$FAPbI_3$ compared to those in the strain-free structure. However, a deceleration of rotation in polar organic molecules is detected in perovskite, instead of the long-range dipole alignment to necessarily generate the ferroelectricity as stated above.

A plausible driving force of the rotation deceleration is change of Hydrogen bond associated with the lattice distortion. The Fourier Transform Infrared Spectroscopy

indicates that the organic molecule rotation has undergone redshift, representing the $FAPbI_3$ unit cell is squeezed that generates an enhancement in Hydrogen bonding between the organic group hydrogen atom and halide part. The enhanced Hydrogen bond thereby impose a higher activation energy barrier for the cation rotations. As the stretched C-N bonding influences the connected Hydrogen bonds, the squeezed unit cell altered the vibration of each molecule; however, although the inorganic atom displacement will deceleration the anisotropy change, ferroelectricity requires a long-range dipole alignment to be necessarily generated. Thus, the ultrafast anisotropy dynamics, together with DFT results indicates that the cation alignments are unlikely to created ordered dipole arrangement to be the main force for the strain-induced ferroelectricity.

To further examine the influence of ferroelectricity corresponding to the inorganic framework, X-ray Photoelectron Spectroscopy (XPS) measurement at lead 4f orbital and iodide 3d orbital is studied as shown in Fig. 3f. The as-grown perovskites are first carried out with biased voltage applied (different poling conditions). After the withdraw of bias voltage, the structure is sent for XPS detection to get rid of the electric field influence that may deform the electronic cloud surrounded the inorganic frameworks since the instantaneous dipole change disappears together with the biased field call off. The as-generated photoelectron binding energy corresponds to the inorganic atom frame shifts obviously, verifying that poling is able to change the relative position of inorganic atoms, which further indicates the displacement in inorganic lead-iodide frames. This displacement results in the ferroelectric nature of strained α-$FAPbI_3$ perovskite.

As such, the organic FA^+ molecule residents inside the lead-iodide lattice are considered to be randomly orientated, and the polar A-site molecule is rotating under

room temperature, which results in a negligible impact on the whole perovskite's ferroelectricity. The strain-dependent ferroelectricity is considered to generate from the atom displacement of inorganic Pb-I bonds.

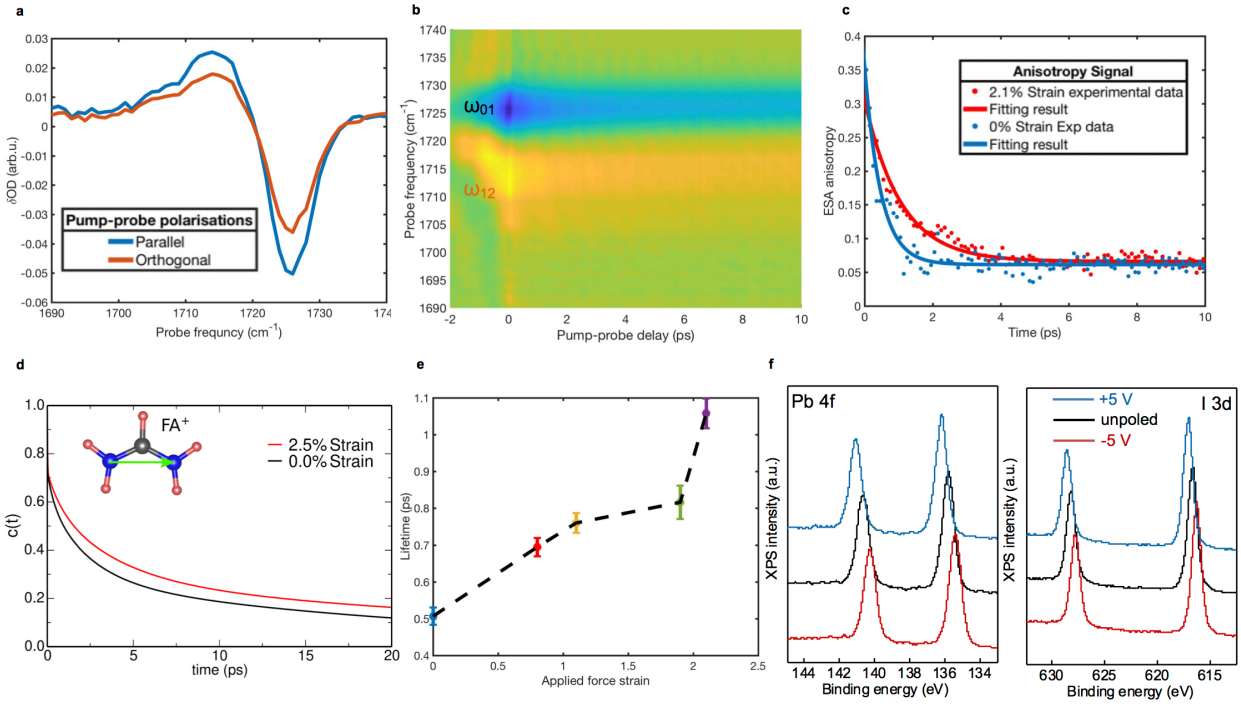

Fig. 3. Ferroelectricity and Molecular Origin a, pump–probe responses of 2.1 in-plane compression of $FAPbI_3$ under parallel and orthogonal pump–probe polarization at t = 0ps. **b,** Parallel pump–probe transient spectra's dynamic of a 2.1 in-plane compression $FAPbI_3$ film measured using broadband excitation. **c,** Transient anisotropy in the peak of GSB/SE response ($1714cm^{-1}$) for samples prepared under 0 force strain and 2.1% force strain. The solid lines represent the transient anisotropy dynamics fitted into one exponential decay. **d,** Vector autocorrelation function c(t) of FA cations for unstrained and 2.5 % strained FAPbI3 perovskite structures from the molecular dynamics simulations. Inset shows the molecular vector of FA+ by an arrow defined by the nitrogen atoms. **e,** Calculated anisotropy decay lifetime under different in-plane compression strain. **f,** XPS measurement for Pb 4f orbital and I 3d orbital. The blue, black and red curve represents the +5V positive bias, non-bias and -5V negative bias applied correspondingly.

6. Conclusion

Through tailoring the composition of metal halide perovskite substrate, in summary, strain is applied to the heteroepitaxal layer due to the lattice mismatch as between, leading to a further epi-phase change from cubic to tetragonal. The strain-induced ferroelectricity is then triggered in the tetragonal α-$FAPbI_3$ single crystalline layer. A switching behavior together with the TSDC field-dependent characterization attributes the ferroelectricity as the result of the phase change and displacement in the strained epitaxial layer. Moreover, the lack of long-range dipole change with the deceleration of cation anisotropy and the inorganic framework displacement lower down the center of ferroelectricity to inorganic bonding within. Synchronously, with the finding of 2D perovskite strain-induced ferroelectricity, our study further solidifies the abundant foreground of strain-ferroelectricity in future studies[34-37].

7. Methods

7.1 Transient IR Absorption

Transiend IR Absorption spectroscopy is applied to investigate anisotropy decay for $FAPbI_3$ under different strain. The setup scheme is shown in Fig. S1. 800-nm laser pulses (~35 fs, ~5 W, 1 kHz) generated by an ultrafast Ti:Sapphire regenerative amplifier (Astrella, Coherent) are sent into an optical parametric amplifier (OPA) (TOPAS, LightConversion) which outputs tunable near-IR pulses. The near-IR pulses are converted to mid-IR pulses through a difference frequency generation (DFG) process by a type II $AgGaS_2$ crystal (Eksma). After DFG, a CaF_2 wedge splits the mid-IR pulse into two parts: the 95% transmitted part is sent into an optical, which forms the pump beam arm; the 5% reflected is the probe beam. Both pump (~ 1.2 μJ) and probe (~ 0.2 μJ) are

focused by a parabolic mirror (f = 10 cm) and overlap spatially at the sample. The output signal is collimated by another parabolic mirror (f = 10 cm) at a symmetric position.

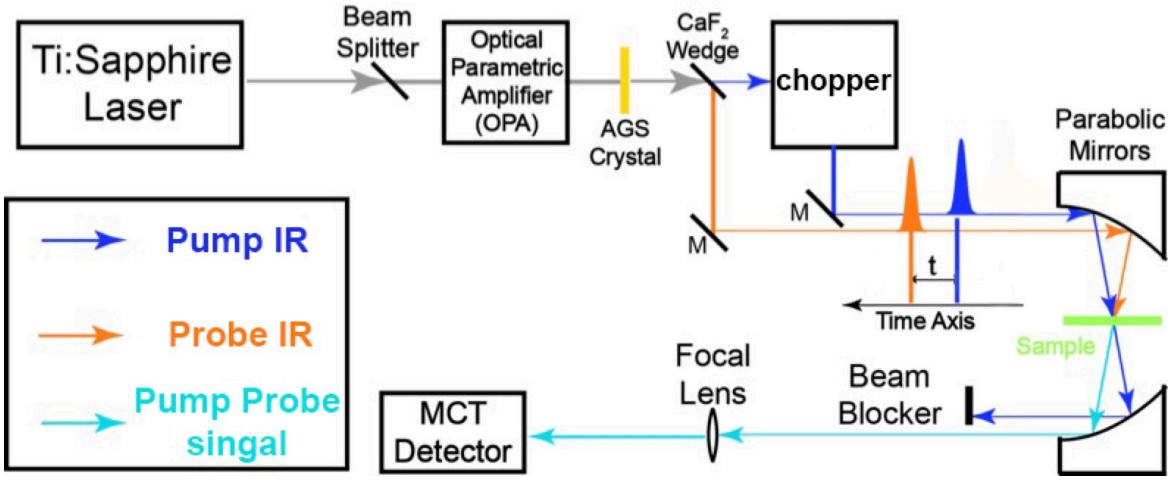

Figure 4: Scheme for Transient IR Absorption in this Study

The pulse sequence is shown in Fig. 2-5. One pump pulses and a probe pulse (pulse duration of 100~150 fs) interact with samples at delayed times (t). After the first IR pulse, a vibrational coherence is generated, after waiting for t, the second IR pulse (probe) is impinged on the sample, and the resulting macroscopic polarization emits an IR signal. The monochromator and MCT (Mercury-Cadmium-Telluride) IR (infrared) Detector (PhaseTech)experimentally Fourier transform the signal, thus generating a spectrum along the probe axis. Numerical Fourier transform of the signal along the t axis is required to obtain the spectrum along probe axis. The t time delay is controlled by a computerized delay stage. The whole data collection process is done by home-written LabVIEW programs.

8. Acknowledgments.

The material in Chapter 2, is currently under preparation for publication with the following authors.: Chen*, Yimu, Zhang Ruiqi*, Chen, Liying, Saiful, Islam, Xiong Wei, Xu Sheng. The thesis author was the secondary investigator and author of this material.

9. References

1. Leng, K., Fu, W., Liu, Y., Chhowalla, M. and Loh, K.P., 2020. From bulk to molecularly thin hybrid perovskites. Nature Reviews Materials, 5(7), pp.482-500.

2. Kim, H.S., Kim, S.K., Kim, B.J., Shin, K.S., Gupta, M.K., Jung, H.S., Kim, S.W. and Park, N.G., 2015. Ferroelectric polarization in CH3NH3PbI3 perovskite. The journal of physical chemistry letters, 6(9), pp.1729-1735

3. Stranks, S.D. and H.J. Snaith, *Metal-halide perovskites for photovoltaic and light-emitting devices.* Nature Nanotechnology, 2015. **10**(5): p. 391-402.

4. Si, H., Zhang, S., Ma, S., Xiong, Z., Kausar, A., Liao, Q., Zhang, Z., Sattar, A., Kang, Z. and Zhang, Y., 2020. Emerging conductive atomic force microscopy for metal halide perovskite materials and solar cells. Advanced Energy Materials, 10(10), p.1903922.

5. Breternitz, J., Lehmann, F., Barnett, S. A., Nowell, H., and Schorr, S. (2020). Role of the iodide–methylammonium interaction in the ferroelectricity of CH3NH3PbI3. Angewandte Chemie International Edition, 59(1), 424-428.

6. Fan, Z., Xiao, J., Sun, K., Chen, L., Hu, Y., Ouyang, J., Ong, K.P., Zeng, K. and Wang, J., 2015. Ferroelectricity of CH3NH3PbI3 perovskite. The journal of physical chemistry letters, 6(7), pp.1155-1161.

7. Rakita, Y., Bar-Elli, O., Meirzadeh, E., Kaslasi, H., Peleg, Y., Hodes, G., Lubomirsky, I., Oron, D., Ehre, D. and Cahen, D., 2017. Tetragonal CH3NH3PbI3 is ferroelectric. Proceedings of the National Academy of Sciences, 114(28), pp.E5504-E5512.

8. Kutes, Y., Ye, L., Zhou, Y., Pang, S., Huey, B. D., and Padture, N. P. (2014). Direct observation of ferroelectric domains in solution-processed CH3NH3PbI3 perovskite thin films. The journal of physical chemistry letters, 5(19), 3335-3339.

9. Garten, L.M., Moore, D.T., Nanayakkara, S.U., Dwaraknath, S., Schulz, P., Wands, J., Rockett, A., Newell, B., Persson, K.A., Trolier-McKinstry, S. and Ginley, D.S., 2019. The existence and impact of persistent ferroelectric domains in MAPbI3. Science advances, 5(1), p.eaas9311.

10. Röhm, H., Leonhard, T., Hoffmann, M. J., and Colsmann, A. (2017). Ferroelectric domains in methylammonium lead iodide perovskite thin-films. Energy & Environmental Science, 10(4), 950-955.

11. Gao, Z.R., Sun, X.F., Wu, Y.Y., Wu, Y.Z., Cai, H.L. and Wu, X.S., 2019. Ferroelectricity of the orthorhombic and tetragonal MAPbBr3 single crystal. The journal of physical chemistry letters, 10(10), pp.2522-2527.

12. Schulz, A. D., Röhm, H., Leonhard, T., Wagner, S., Hoffmann, M. J., and Colsmann, A. (2019). On the ferroelectricity of CH3NH3PbI3 perovskites. Nature materials, 18(10), 1050-1050.

13. Wang, P., Zhao, J., Wei, L., Zhu, Q., Xie, S., Liu, J., Meng, X. and Li, J., 2017. Photo-induced ferroelectric switching in perovskite CH3NH3PbI3 films. Nanoscale, 9(11), pp.3806-3817.

14. Liu, Y., Collins, L., Proksch, R., Kim, S., Watson, B.R., Doughty, B., Calhoun, T.R., Ahmadi, M., Ievlev, A.V., Jesse, S. and Retterer, S.T., 2018. Chemical nature of ferroelastic twin domains in CH3NH3PbI3 perovskite. Nature materials, 17(11), pp.1013-1019.

15. Xiao, X., Li, W., Fang, Y., Liu, Y., Shao, Y., Yang, S., Zhao, J., Dai, X., Zia, R. and Huang, J., 2020. Benign ferroelastic twin boundaries in halide perovskites for charge carrier transport and recombination. Nature communications, 11(1), pp.1-7.

16. Gómez, A., Wang, Q., Goñi, A.R., Campoy-Quiles, M. and Abate, A., 2019. Ferroelectricity-free lead halide perovskites. Energy & Environmental Science, 12(8), pp.2537-2547.

17. Liu, Y., Collins, L., Proksch, R., Kim, S., Watson, B.R., Doughty, B., Calhoun, T.R., Ahmadi, M., Ievlev, A.V., Jesse, S. and Retterer, S.T., 2019. Reply to: On the ferroelectricity of CH3NH3PbI3 perovskites. Nature materials, 18(10), pp.1051-1053.

18. Röhm, H., Leonhard, T., Hoffmann, M.J. and Colsmann, A., 2020. Ferroelectric poling of methylammonium lead iodide thin films. Advanced Functional Materials, 30(5), p.1908657.

19. Guo, H., Liu, P., Zheng, S., Zeng, S., Liu, N. and Hong, S., 2016. Re-entrant relaxor ferroelectricity of methylammonium lead iodide. Current Applied Physics, 16(12), pp.1603-1606.

20. Chen, Y., Lei, Y., Li, Y., Yu, Y., Cai, J., Chiu, M.H., Rao, R., Gu, Y., Wang, C., Choi, W. and Hu, H., 2020. Strain engineering and epitaxial stabilization of halide perovskites. Nature, 577(7789), pp.209-215.

21. Hong, Z., Zhao, J., Huang, K., Cheng, B., Xiao, Y. and Lei, S., 2019. Controllable switching properties in an individual CH3NH3PbI3 micro/nanowire-based

transistor for gate voltage and illumination dual-driving non-volatile memory. Journal of Materials Chemistry C, 7(14), pp.4259-4266.

22. Wei, H., Yang, Y., Chen, S. and Xiang, H.J., 2021. Lead-free hybrid perovskite N (CH3)4SnI3 with robust ferroelectricity induced by large and non-polar N(CH3)4+ molecular cation. Nature communications, 12(1), pp.1-8.

23. Huang, B., Kong, G., Esfahani, E.N., Chen, S., Li, Q., Yu, J., Xu, N., Zhang, Y., Xie, S., Wen, H. and Gao, P., 2018. Ferroic domains regulate photocurrent in single-crystalline CH3NH3PbI3 films self-grown on FTO/TiO2 substrate. npj Quantum Materials, 3(1), pp.1-8.

24. Zhang, H.Y., Song, X.J., Cheng, H., Zeng, Y.L., Zhang, Y., Li, P.F., Liao, W.Q. and Xiong, R.G., 2020. A three-dimensional lead halide perovskite-related ferroelectric. Journal of the American Chemical Society, 142(10), pp.4604-4608.

25. Morozov, M., *Softening and hardening transitions in ferroelectric Pb(Zr,Ti)O3 ceramics*. EPFL.

26. Wilson, J.N., Frost, J.M., Wallace, S.K. and Walsh, A., 2019. Dielectric and ferroic properties of metal halide perovskites. APL Materials, 7(1), p.010901.

27. Zhang, H.Y., Chen, X.G., Zhang, Z.X., Song, X.J., Zhang, T., Pan, Q., Zhang, Y. and Xiong, R.G., 2020. Methylphosphonium Tin Bromide: A 3D Perovskite Molecular Ferroelectric Semiconductor. Advanced Materials, 32(47), p.2005213.

28. Sewvandi, G.A., Kodera, K., Ma, H., Nakanishi, S. and Feng, Q., 2016. Antiferroelectric Nature of CH3NH3PbI3−xClx Perovskite and Its Implication for Charge Separation in Perovskite Solar Cells. Scientific reports, 6(1), pp.1-6.

29. Vorpahl, S.M., Giridharagopal, R., Eperon, G.E., Hermes, I.M., Weber, S.A. and Ginger, D.S., 2018. Orientation of ferroelectric domains and disappearance upon heating methylammonium lead triiodide perovskite from tetragonal to cubic phase. ACS Applied Energy Materials, 1(4), pp.1534-1539.

30. Whitfield, P.S., Herron, N., Guise, W.E., Page, K., Cheng, Y.Q., Milas, I. and Crawford, M.K., 2016. Structures, phase transitions and tricritical behavior of the hybrid perovskite methyl ammonium lead iodide. Scientific reports, 6(1), pp.1-16.

31. Tan, H.-S., I.R. Piletic, and M.D. Fayer, *Polarization selective spectroscopy experiments: methodology and pitfalls.* Journal of the Optical Society of America B, 2005. **22**(9): p. 2009-2017.

32. Bakulin, A.A., Selig, O., Bakker, H.J., Rezus, Y.L., Müller, C., Glaser, T., Lovrincic, R., Sun, Z., Chen, Z., Walsh, A. and Frost, J.M., 2015. Real-time observation of

organic cation reorientation in methylammonium lead iodide perovskites. The journal of physical chemistry letters, 6(18), pp.3663-3669.

33. Taylor, V.C., Tiwari, D., Duchi, M., Donaldson, P.M., Clark, I.P., Fermin, D.J. and Oliver, T.A., 2018. Investigating the role of the organic cation in formamidinium lead iodide perovskite using ultrafast spectroscopy. The journal of physical chemistry letters, 9(4), pp.895-901.

34. Hou, Y., Wu, C., Yang, D., Ye, T., Honavar, V.G., Van Duin, A.C., Wang, K. and Priya, S., 2020. Two-dimensional hybrid organic–inorganic perovskites as emergent ferroelectric materials. Journal of Applied Physics, 128(6), p.060906.

35. Ma, W., Zhang, X., Xu, Z., Guo, H., Lu, G. and Meng, S., 2020. Reducing anomalous hysteresis in perovskite solar cells by suppressing the interfacial ferroelectric order. ACS applied materials & interfaces, 12(10), pp.12275-12284.

36. Haeni, J.H., Irvin, P., Chang, W., Uecker, R., Reiche, P., Li, Y.L., Choudhury, S., Tian, W., Hawley, M.E., Craigo, B. and Tagantsev, A.K., 2004. Room-temperature ferroelectricity in strained SrTiO 3. Nature, 430(7001), pp.758-761.

37. Leng, K., Fu, W., Liu, Y., Chhowalla, M. and Loh, K.P., 2020. From bulk to molecularly thin hybrid perovskites. Nature Reviews Materials, 5(7), pp.482-500.

10 Supplemental Information

10.1 Wobbling in a Cone/Jump motion

Although one exponential plus a constant model could fit the anisotropy decay with good precision ($R^2 > 0.947$), most available experiments address cation dynamics in metal halide perovskite into a two-time scale picture, using a biexponetial model.[1-4] The anisotropy data for the $FAPbI_3$ with 0% strain and 2.1% strain are fitted well into a biexponential model ($R^2 > 0.954$). The biexponential fitting model for R(t) is given by the equation. 2:[5]

$$R(t) = \frac{2}{5}(S^2 \exp\left(-\frac{t}{\tau_{jump}}\right) + (1 - S^2) \exp\left(-\frac{t}{\tau_{fast}}\right)) \quad (2)$$

and were R(t) is the anisotropy, S^2 is the generalized order parameter that describes the degree of restriction on the wobbling-in-the-cone orienational motion. The time constant of the final diffusive full orientational relaxation is denoted by τ_{jump}, which can occur through jump reorientation mechanism.[6] And τ_{fast} can be correlate to τ_{wobble} which is the time constant that describes the wobbling-in-the-cone motion using the equation. 3:[7]

$$\tau_{wobble}{}^{-1} = (\tau_{fast}{}^{-1} - \tau_{jump}{}^{-1})^{-1} \quad (3)$$

In this model, two motions take place: wobbling-in-a-cone motions followed by jump reorientation.[8] In SI figure 1, we compute τ_{fast}, τ_{jump}, and τ_{wobble} under different in-plane compression, respectively. For the time scale for the overall orientational relaxation for stain free case (τ_{jump}), it is too long to fit and have a relatively big standard deviation, which validate the single exponential plus a constant model, i.e. the constant is an

exponential with infinite lifetime. However, we can quantitatively conclude as compression as the strain force increased from 0 to 2.1%, τ_{slow} decreased from 40 ± 20 ps to 4.7 ± 0.4 ps and τ_{wobble} increased from 0.4 ± 0.2 ps to 0.67 ± 0.2 ps. From XRD result, strain applied and lattice transform from cubic to tetragonal, PbI_6 frame transit might be distorted and such distortion will decrease the stability of the hydrogen bond network, i.e. hydrogen bond can be broken more frequently and thereby enhance hydrogen bond fluctuation.[9] Such enhancement could reduce the lifetime for τ_{jump} motion which might be a possible explanation for the decreasing trend we observe in SI figure 1. To better understanding the wobbling in the cone motion, we compute the cone semiangle θ using equation. 4:[10]

$$S^2 = [\frac{1}{2}(cos\theta)(1 + cos\theta)]^2 \quad (4)$$

and the wobbling in a cone diffusion constant D_c is compute using equation .5:[10]

$$D_c = \frac{{x_c}^2(1+x_c)^2\left\{\ln\left[\frac{1+x_c}{2}\right]+\frac{1-x_c}{2}\right\}}{\tau_{wobble}(1-S^2)[2(x_c-1)]} + \frac{(1-x_c)(6+8x_c-1-{x_c}^2-12{x_c}^3-7{x_c}^4)}{24\tau_{wobble}(1-S^2)} \quad (5)$$

where $x_c = cos\theta$. From figure 17, when strain applied, the cone angle reduced from 55.7° ± 1.1° to 48° ± 2°. From XRD result, as the in-plane compression increase from 0 to 2.1%, the a, b axis be compressed and c axis elongated, the semicone angle would be further confine as the lattice confine, which is consistent with the experimental observation in figure 17. Consequently, the smaller cone angle confines the FA cations, restricting their rotational degrees of freedom within the smaller cone. However, the

rotational diffusion constant (Supplementary Fig.18) also decreases due to the stronger Hydrogen bond. The net result is that the fast anisotropy decay slows down when the strain is applied compared to that of the strain-free structure. Quantitatively, from 0% to 2.1% strain, wobbling in a cone life time become longer. As mentioned in DFT calculation and FTIR result, the possible driving force of a slower wobbling in the cone rotational rate is the hydrogen bonding strength between the H on FA cation and I on Pb-I cage, which is likely to enhance when strain applied. Therefore, as figure 16 shows, when compression strain applied, the wobbling in a cone motion would have a slower decay dynamic.

SI 1

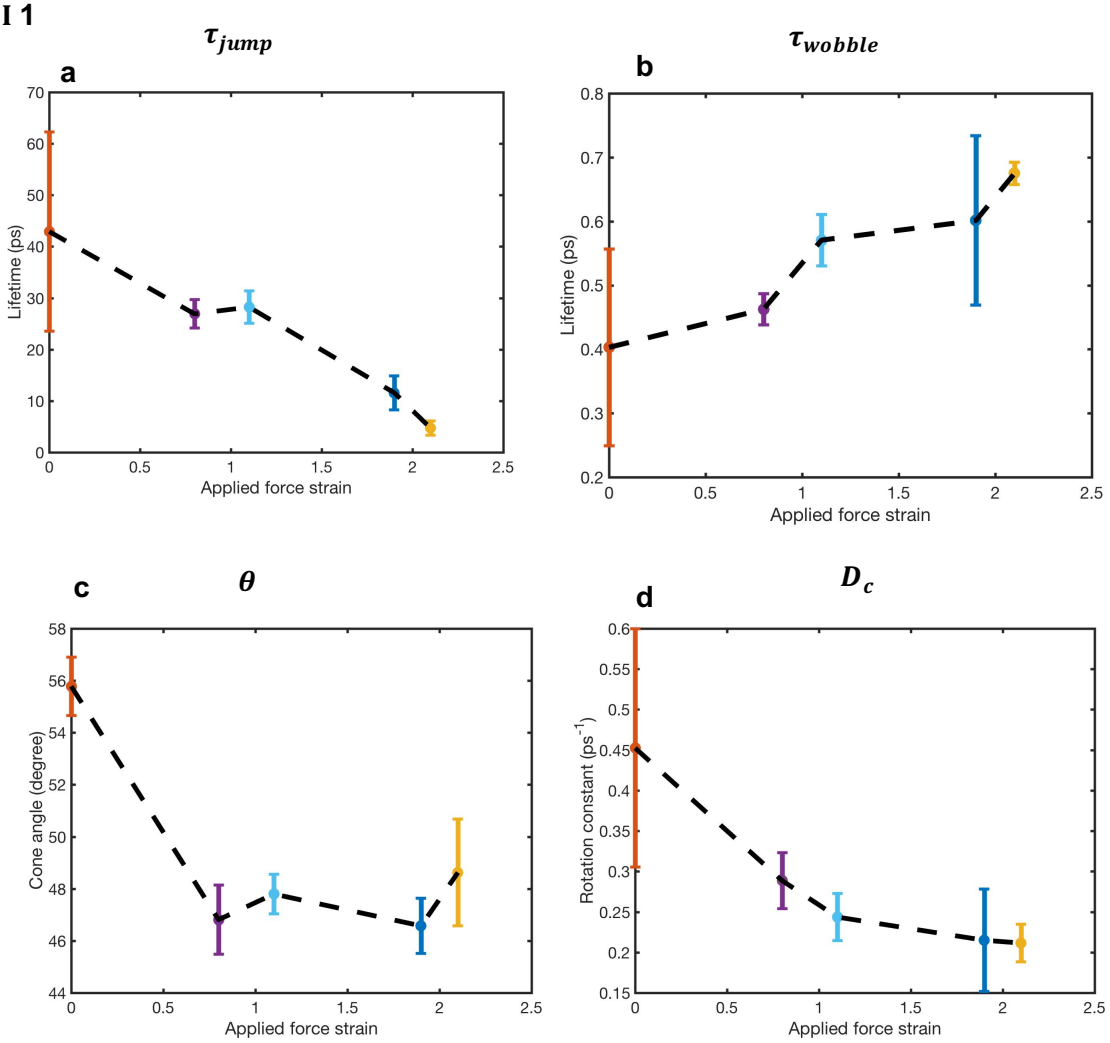

Supplementary Fig. 1 | Calculated anisotropy decay lifetime in shot time scale, fast time scale, cone angle, diffusion rotation constant under different in-plane compression strain.

10.2 SI References

1. Howe-Siang Tan, Ivan R. Piletic and M. D. Fayer, “Polarization Selective Spectroscopy Experiments: Methodology and Pitfalls,”, J.O.S.A. B 22, 2009-2017 (2005).

2. Bakulin, Artem A., Oleg Selig, Huib J. Bakker, Yves LA Rezus, Christian Müller, Tobias Glaser, Robert Lovrincic et al. "Real-time observation of organic cation reorientation in methylammonium lead iodide perovskites." The journal of physical chemistry letters 6, no. 18 (2015): 3663-3669.

3. Taylor, Victoria CA, Devendra Tiwari, Marta Duchi, Paul M. Donaldson, Ian P. Clark, David J. Fermin, and Thomas AA Oliver. "Investigating the role of the organic cation in formamidinium lead iodide perovskite using ultrafast spectroscopy." The journal of physical chemistry letters 9, no. 4 (2018): 895-901.

4. Gallop, Nathaniel P., Oleg Selig, Giulia Giubertoni, Huib J. Bakker, Yves LA Rezus, Jarvist M. Frost, Thomas LC Jansen, Robert Lovrincic, and Artem A. Bakulin. "Rotational cation dynamics in metal halide perovskites: Effect on phonons and material properties." The journal of physical chemistry letters 9, no. 20 (2018): 5987-5997.

5. Quitevis, Edward L., Andrew H. Marcus, and Michael D. Fayer. "Dynamics of ionic lipophilic probes in micelles: picosecond fluorescence depolarization measurements." The Journal of Physical Chemistry 97, no. 21 (1993): 5762-5769.

6. Ji, Minbiao, Michael Odelius, and K. J. Gaffney. "Large angular jump mechanism observed for hydrogen bond exchange in aqueous perchlorate solution." Science 328, no. 5981 (2010): 1003-1005.

7. Tan, Howe-Siang, Ivan R. Piletic, and M. D. Fayer. "Orientational dynamics of water confined on a nanometer length scale in reverse micelles." The Journal of chemical physics 122, no. 17 (2005): 174501.

8. Shin, Jae Yoon, Yong-Lei Wang, Steven A. Yamada, Samantha T. Hung, and Michael D. Fayer. "Imidazole and 1-Methylimidazole Hydrogen Bonding and Nonhydrogen Bonding Liquid Dynamics: Ultrafast IR Experiments." The Journal of Physical Chemistry B 123, no. 9 (2019): 2094-2105.

9. Luzar, Alenka, and David Chandler. "Structure and hydrogen bond dynamics of water–dimethyl sulfoxide mixtures by computer simulations." The Journal of chemical physics 98, no. 10 (1993): 8160-8173.

10. Lipari, Giovanni, and Attila Szabo. "Effect of librational motion on fluorescence depolarization and nuclear magnetic resonance relaxation in macromolecules and membranes." Biophysical journal 30, no. 3 (1980): 489-506.

Chapter 3 Ultrafast interfacial charge transfer revealed by transient vibrational sum frequency generation spectroscopy

1. Introduction

Photon induced charge transfer are fundamental processes in nature and affects the efficiency and performance of many important application, such as molecular light-harvesting materials, organic flexible electronics, and selectivity and activities of photo catalysts[1,2]. Unlike most charge transfer events involve intermediate states and multiple steps, a direct charge transfer can vertically excite charges from their initial electronic states at donor molecules to the unoccupied electronic states of acceptors which would increase the efficiency of charge transfer process.[3] However, only interfaces between small molecules and metal shows direct charge transfer.[4] There were several challenges to study this process, such as, probing interfacial charge transfer needs characterization methods to be interface-sensitive, the spectroscopy technique needs to be molecular vibrational specificity, and charge transfer happens within ultrafast time scale. Previously, our group has implemented transient vibrational sum frequency generation (VSFG) spectroscopy, and provide spectroscopic evidence of direct electron transfer at complex polymer/metal interfaces and further understand molecular conformation–charge dynamic relationships.[5] Based on our group's previous work, we would like to study whether direct charge transfer exists in complex interface, such as organic/inorganic, organic/organic interface. Therefore, we aim to develop time-resolved electric-field-induced sum-frequency generation (Tr EFI SFG) and develop time-resolved electric-field-induced heterodyne sum frequency (Tr EFI-HD SFG) spectroscopy to overcome the challenges mentioned above. Tr EFI SFG takes advantage of the electric-field-induced effect to measure the transient current (DC) field

at interfaces due to charge transfer. Simultaneously, the vibrational spectra feature of VSFG reveals molecular conformation information. By fitting the pump-probe spectrum's temporal trace, we can separate direct charge transfer and indirect charge transfer because of different pathways. In Tr EFI SFG, the static and transient VSFG spectra are composed of both non-resonant (NR) and resonant molecular responses. Through Tr EFI-HD SFG and after global analysis and phase rotation, the imaginary part of HD transient spectra can be transformed into pure molecular response and separated into different components. By doing so, we can identify different types of molecular dynamics at interfaces, such as coherent artifact, charge recombination, and charge separation which is important to improve the OPV performance.

Here, we study the model interface that comprised of high-electron-affinity acceptor polymer (BBL) and low-ionization-energy donor polymer (P3HT) for organic/organic heterojunction. We choose this system since from band alignment in figure. 1[6], if the pump light can trigger the charge transfer from HOMO orbital of P3HT to LUMO of BBL, we will confirm the charge transfer happens at interface. Also, P3HT and BBL is relatively stable and keep their functions within 4 days under air condition which would make our measurement easier.

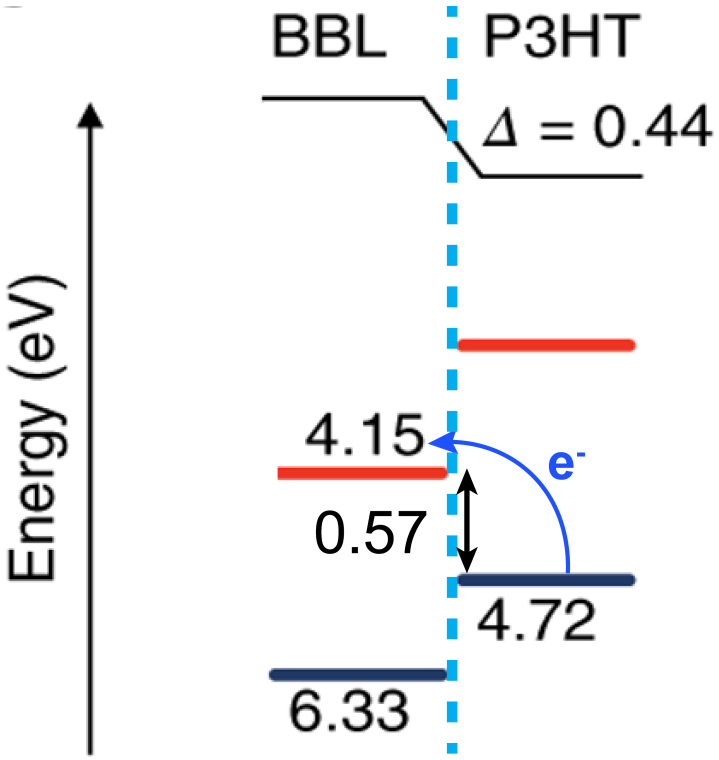

Figure.1 Band alignment for P3HT and BBL

2. Current result

We performed Tr EFI SFG using 3000 cm^{-1} mid-IR to monitor C-H stretching if P3HT and a 1030 nm pulse are used as the pump to trigger charge transfer. The time-resolved SFG dynamic can be described as follows: after an initial negative signal at t=0, the overall SFG signal recovers and shows a negative pump-probe signal. (Figure. 2a). To rule out other nonlinear processes, such as P3HT two-photon absorption, we perform a pump power-dependent control experiments. By incrementing pump power, information on charge dynamic power dependence is shown in figure. 2b. The preliminary results show that pump power and Tr- SFG signal share a first-order relationship, which indicates that the signal we observed is a one photon process.

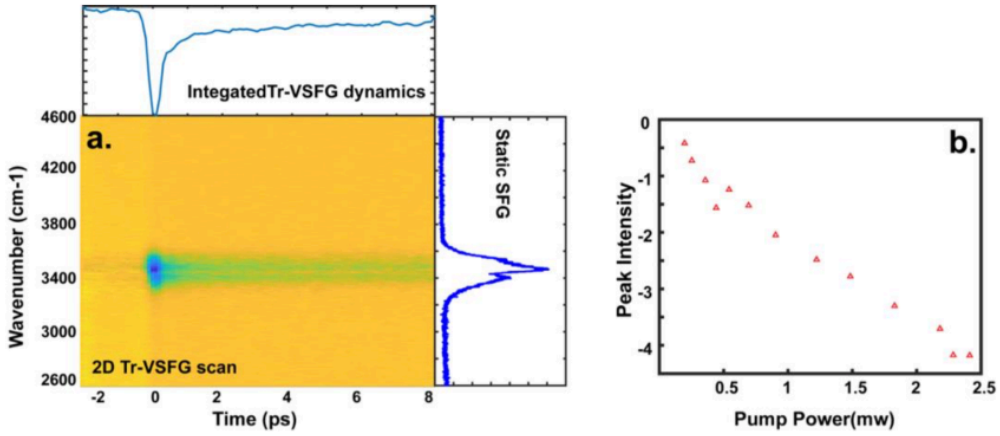

Figure 2. (a) 2D tr-VSFG spectrum. A negative signal is observed at t=0 ps, which recovers very fast and becomes a negative peak at t>0 ps. Top: Integrated tr-VSFG signal. Right: linear VSFG spectrum. (b) Pump-probe intensity with pump power

Using global analysis, we could break down the overall dynamic into three components. Currently, we suspect that component 1,2 and 3 are corresponding to coherent artifact, charge recombination, and charge transfer, respectively.

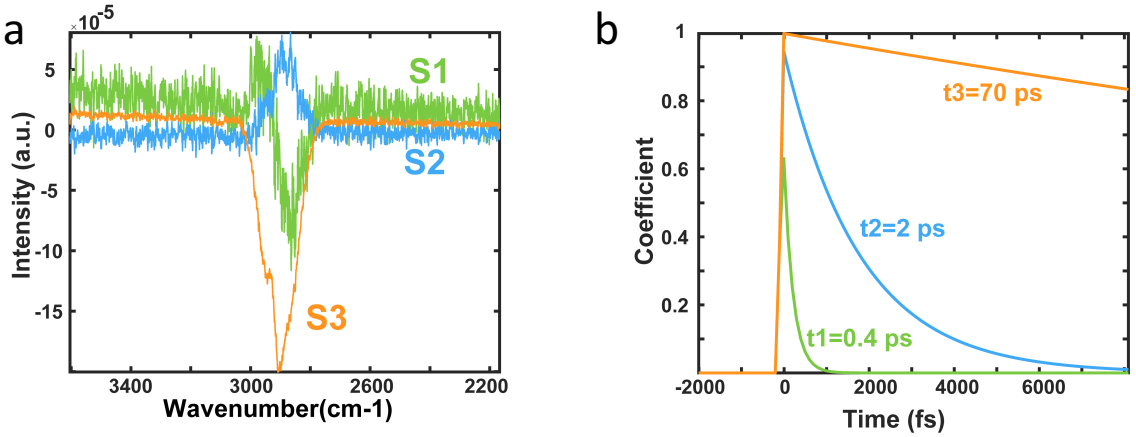

Figure 3. (a) Global analysis separated peak component. (b) Dynamic of corresponding

3.Future Goal

Building on Tr EFI SFG, we would like to build a Tr EFI-HD SFG to extract the implicit molecular dynamics. The design of the proposed time-resolved EFI-HD SFG spectrometer is shown in Figure 3[5]

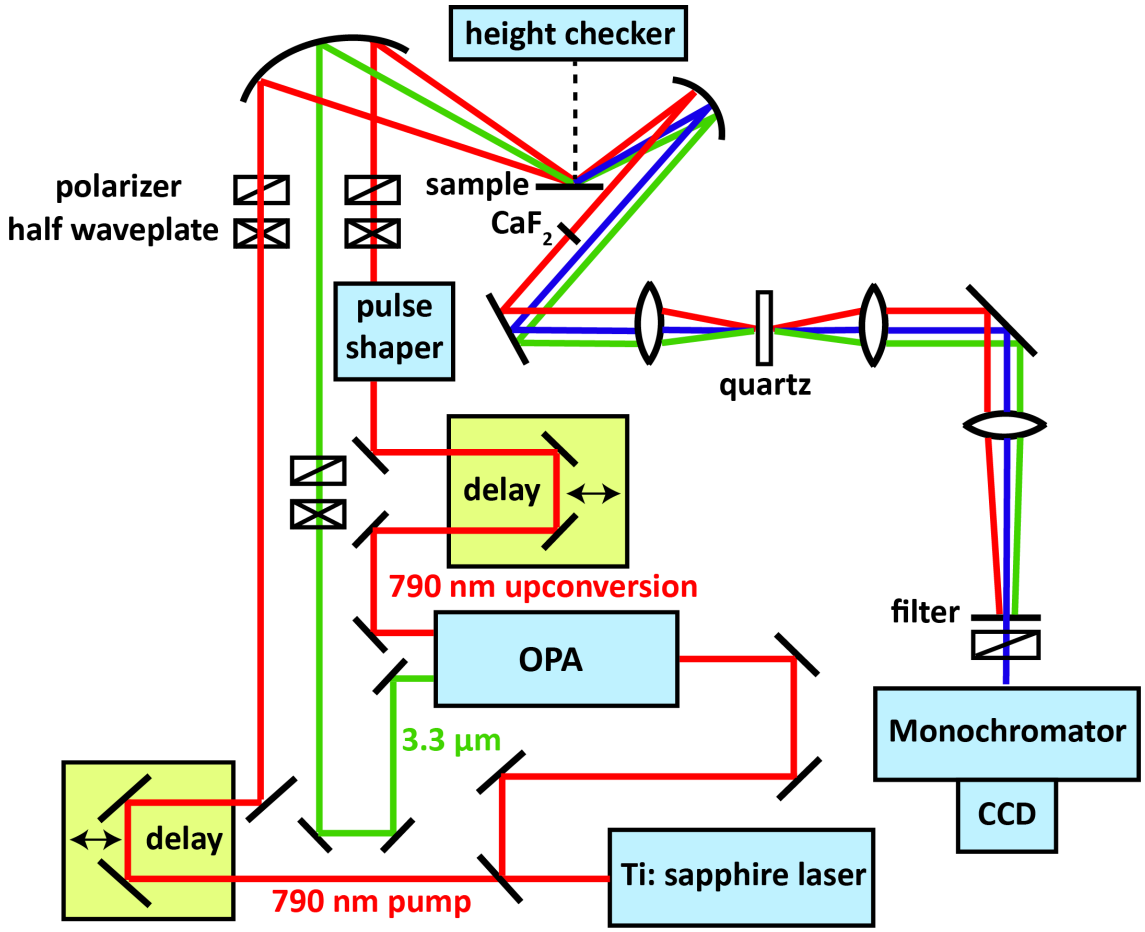

Figure 4. Schematic of the transient HD VSFG spectrometer setup.

The VSFG probe signal is arranged collinearly with another laser pulse with the same frequency, known as a local oscillator (LO), to create the interference and, therefore,

heterodyne detection. Heterodyne detection can improve the signal-to-noise ratio for studying submonolayer interfaces. To extract time-dependent molecular dynamics from the convoluted transient VSFG measurement with large NR signal[7], first we check the NR spectral phase being consistent while the molecular resonance phase is frequency-dependent. We could perform phase rotation and global analysis method to extract molecular dynamic.[5] From this experiment, we could learn how the acceptor molecules are involved in charge dynamics at the interface and how the electronic dipole interacts with the charge separation process.

In the future, we also would like to find some method such as some solvent that could dissolve both polymer and make a bulk heterojunction instead of the planar heterojunction that we were observing. With bulk heterojunction, we could use a near-IR pulse to directly induce the charge transfer and observe corresponding process.

4. Acknowledgments.

The material in Chapter 3, is an ongoing project with following people: Wang, Chenglai, Chen, Liying under Dr Xiong, W's guidance.

5. References

1. Schäfer, C., Ruggenthaler, M., Appel, H. and Rubio, A., 2019. Modification of excitation and charge transfer in cavity quantum-electrodynamical chemistry. Proceedings of the National Academy of Sciences, 116(11), pp.4883-4892.

2. Srimuk, P., Su, X., Yoon, J., Aurbach, D. and Presser, V., 2020. Charge-transfer materials for electrochemical water desalination, ion separation and the recovery of elements. Nature Reviews Materials, 5(7), pp.517-538.

3. Wu, K., Chen, J., McBride, J.R. and Lian, T., 2015. Efficient hot-electron transfer by a plasmon-induced interfacial charge-transfer transition. Science, 349(6248), pp.632-635.

4. Jailaubekov, A.E., Willard, A.P., Tritsch, J.R., Chan, W.L., Sai, N., Gearba, R., Kaake, L.G., Williams, K.J., Leung, K., Rossky, P.J. and Zhu, X.Y., 2013. Hot charge-transfer excitons set the time limit for charge separation at donor/acceptor interfaces in organic photovoltaics. Nature materials, 12(1), pp.66-73.

5. Xiang, B., Li, Y., Pham, C.H., Paesani, F. and Xiong, W., 2017. Ultrafast direct electron transfer at organic semiconductor and metal interfaces. Science advances, 3(11), p.e1701508.

6. Xu, K., Sun, H., Ruoko, T.P., Wang, G., Kroon, R., Kolhe, N.B., Puttisong, Y., Liu, X., Fazzi, D., Shibata, K. and Yang, C.Y., 2020. Ground-state electron transfer in all-polymer donor–acceptor heterojunctions. Nature materials, 19(7), pp.738-744.

7. Wang, C., Li, Y. and Xiong, W. Extracting molecular responses from ultrafast charge dynamics at material interfaces. J. Mater. Chem. C 8, 12062–12067 (2020).